Trapping of Yb+ Loaded through Photoionization in RF Ion Trap(Dissertation_全文)

AUTHOR(S):

Onoda, Yugo

Trapping of Yb^+ Loaded through Photoionization in RF Ion Trap

(光イオン化法で生成した Yb^+ の RF イオントラップ)

Yugo ONODA

2011

Abstract

In this thesis, we present our study on loading of Yb^+ ions produced by photoionization into a radio frequency (RF) trap. Yb^+ is one of the attractive ion species for use in optical frequency standards and quantum information processing. Photoionization is recently applied as a method of loading of ions into the ion trap, because it has some advantages such as high efficiency and isotope-selectivity. Photoionization loading of Yb^+ ions has been already used in several studies. However, a detailed investigation of the loading has not been conducted so far. We measure the loading rate by using the electric resonance detection of the secular motion of the trapped Yb^+ ions. They are cooled with a helium buffer gas. Unlike the measurement using the ions trapped with help of laser cooling, we remove the effect of the cooling efficiency from the loading rate owing to high efficiency of buffer-gas cooling. From the electric resonance signal, one can estimate the number of trapped ions. We can determine the loading cross section by using the estimated ion number. The loading cross section enables us to compare the results with those obtained in other systems.

Before we measure the loading rate, we improve the method of number estimation from the electric resonance signal, and we prepare light sources for photoionization. As the improvement of the number estimation, we decrease the uncertainty in the number estimation to be approximately 10% even in the presence of anharmonicity, when the relative signal height is smaller than 0.3. This is essential because the anharmonicity accompanies the usual trap design and causes a hysteresis in the electric resonance signal.

For the light source, we obtain the results not only useful for our investigation of the loading rate but also applicable to other studies using various atoms and ions. We need to develop a single-frequency and continuously frequency tunable light source at 399 nm, with which the $^1S_0 - {}^1P_1$ transition in Yb atoms is driven as the first-excitation of the photoionization, in order to use the light source in a future application of the

isotope-selective loading. The radiation that we first developed is second-harmonics of a continuous-wave (CW) titanium-sapphire-laser radiation. In order to enhance the conversion efficiency in second harmonic generation of the CW laser that usually has small output power, a nonlinear crystal that generates second harmonics is placed in the external cavity. When an antireflection-coated normal-cut nonlinear crystal is used in an external cavity, a small residual reflection at the crystal facets causes a round-trip loss and prevents the realization of a large fundamental enhancement. This problem is eliminated when the reflected beams at the crystal facets are subject to constructive interference. We demonstrate that the temperature tuning of a β-BaB_2O_4 crystal is effective to realize constructive interference at any wavelength. The radiation that we secondly developed is that of an extended-cavity laser diode (ECLD) using a high-power ultraviolet diode chip that is very recently available. We achieve a single-frequency oscillation even at the maximum operation power of the chip, when the cavity length of the ECLD is shortened. A precise frequency tuning is required for the isotope-selective loading using the isotope shifts in the transition used as the first excitation of photoionization. We demonstrate a simple method to detect minor isotope lines in a saturated absorption spectrum by absorption filtering of major isotope lines. We investigate this method for the spectroscopy of the $^1S_0 - {}^1P_1$ transition in Yb by controlling the density of Yb atoms by varying the discharge current of a hollow cathode lamp. We selectively detect the lines of the useful isotope of 171 and of the isotope of the smallest natural abundance of 168.

As the main study of this thesis, we investigate the photoionization loading into a RF trap, in particular, the loading rate by two-color and one-color photoionizations and the effect of the charge exchange collision on the isotope-selective loading. In two-color photoionization, where the first-excitation laser drives the $^1S_0 - {}^1P_1$ transition in the Yb atom and the second one ionizes the atom from the $^1P_1$ state, we measure the dependence of the second-excitation wavelength. That the loading rate is at its highest by the excitation of the ionization potential. A similar loading rate is observed at the second-laser wavelength around 369.5 nm, which is the wavelength for the cooling transition of Yb^+. Thus we quantitatively confirm that the cooling laser of Yb^+ is a good substitute for the second-excitation laser. The excitation of the Yb atoms in the Rydberg states is detected by the enhancement of the loading rate. By irradiation with only the first-excitation laser, i.e., in one-color excitation, Yb^+ is produced at a rate three orders of magnitude

smaller than that in two-color excitation of the ionization potential, as the non-resonant two-photon absorption from the $^1P_1$ state is the dominant process. Using the number estimation method that we improve, we determine the number loading rate. And then, we estimate the loading cross section to be 40(15) Mb for the two-color excitation of the ionization potential. Because we improve the uncertainty in the number estimation, the uncertainty in the loading cross section is limited by those in the estimations of other parameters such as the density of Yb atoms. Because the ionization region is smaller than the trap region and an efficient buffer-gas cooling is combined, our method could be a useful one for measurement of the rate and cross section of photoionization. We also measure the charge-exchange rate between Yb^+ and Yb atoms from the oven by using two enriched isotopes. We discuss its effect on isotope-selective photoionization loading by using the rates of the photoionization loading and the charge exchange that we estimate. We conclude that the charge exchange is a significant factor in limiting the number of target isotope ions that are purely isotope-selectively loaded, only for the target isotope of its abundance smaller than 0.1%, i.e., the rarest isotope of 168 in the natural isotope mixture, in our photoionization scheme of Yb. The loading duration is required to be much smaller than the inverse of the charge exchange rate.

Contents

Chapter 1

Introduction

1.1 Background

Ion trap technique is one of the methods to provide reference frequencies used in optical frequency standards. Confinement of atoms within the order of the wavelength, i.e., the Lamb-Dicke regime, eliminates the first-order Doppler shift. Applying laser cooling to the trapped ions enables us to achieve the Lamb-Dicke confinement of the optical wavelength. A fractional frequency instability of the optical frequency standard is expected to be improved by a factor of 10^4, from that of the frequency standard at present, defined in microwave by the transition between the hyperfine structures of the ground state in cesium. In single-ion optical clocks, an uncertainty of the order of 10^{-18} in the frequency is predicted and has been demonstrated very recently [1], because they are insensitive to the perturbations which shift the transition frequencies. Singly ionized ytterbium ion (Yb^+) is one of the suitable ion species for use in optical frequency standards [2,3], and is also applied to a qubit in quantum information processing [4]. Yb^+ has energy levels like alkali-metal atoms. The partial energy diagram is shown in Fig. 1.1. The transition used for laser cooling and optical detection is the $^2S_{1/2} - {}^2P_{1/2}$ transition at 370 nm. In order to continue the cooling cycle, the $^2D_{3/2} - {}^3D[3/2]_{1/2}$ transition at 935 nm is driven to deplete the $^2D_{3/2}$ metastable state. The odd isotopes of Yb^+ have magnetic sublevels of $m_F = 0$ which have no first-order Zeeman shift. Therefore, the transitions between $m_F = 0$ and $m'_F = 0$ are suitable as clock transitions. The odd isotopes have an disadvantage that they have hyperfine structures and a scheme of laser cooling is more complicated than that for

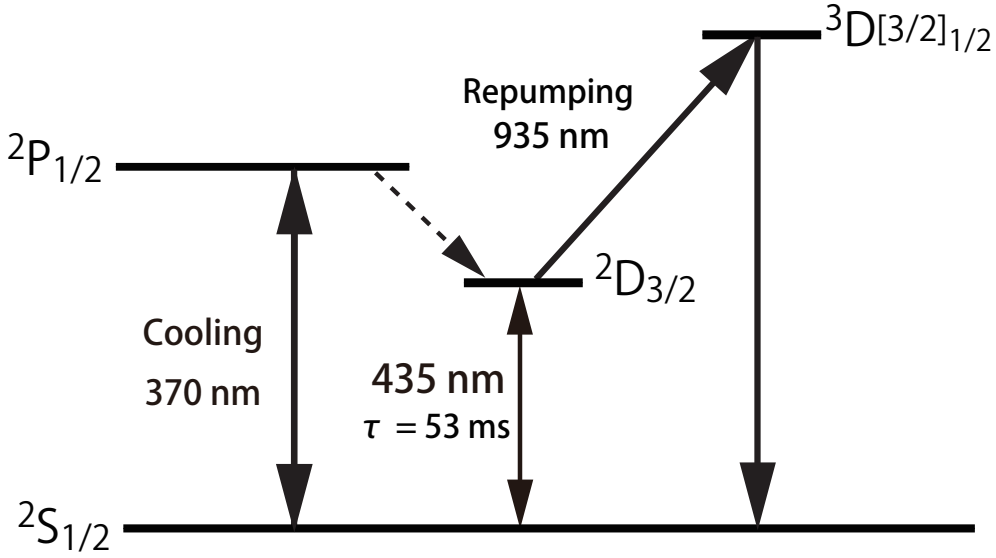

Fig. 1.1 Partial energy diagram of Yb^+.

the even isotopes that have no hyperfine structures. In the odd isotopes of Yb^+, $^{171}Yb^+$ is the most attractive because it has relatively simple hyperfine structures because of the nuclear spin of 1/2. The natural abundances of the stable isotopes of Yb are shown in Table 1.1 [5].

In the ion trap technique, loading ions into the trap is required as the first step. The trapped ions are usually loaded through ionization of neutral atoms inside the trap region. Electron-impact ionization is conventionally used for this purpose. Recently, photoionization has been widely used because it offers the following advantages [6–10]: (i) It is free from electrons, which stick on insulators supporting the trap electrodes and thus generate stray DC fields that enlarge the micromotion. (ii) It has higher ionization efficiency than electron impact ionization. This enables us to decrease the density of neutral atoms to be ionized, thus, suppressing the generation of a patch potential between the electrode surface and the neutral atoms deposited on it. This patch potential also enlarges the micromotion. (iii) Photoionization offers isotope-selective loading through the isotope shifts in the intermediate states. (iv) Finally, it also leads to fluorescence of trapped ions during the loading process. This enables us to load ions one by one.

In the photoionization loading of Yb^+, the $^1S_0 - ^1P_1$ transition at 399 nm in Yb atoms is used as the first excitation and the isotope selection. The energy diagram of Yb for

Table. 1.1 Natural abundances of stable isotopes of Yb atoms.

Mass number	Natural abundance / %
168	0.1
170	3
171	14
172	22
173	16
174	32
176	13

the photoionization conducted in this thesis is shown in Fig. 1.2. In the first report of the photoionization loading of Yb^+ [11], only the radiation at 399 nm was used. We refer to this photoionization as one-color photoionization in this thesis. Subsequently, two-color photoionization was reported, where simultaneous irradiation with light at 370 nm, which drives the $^2S_{1/2} - ^2P_{1/2}$ cooling transition in Yb^+, increased loading efficiency by a factor of 10 [10]. Although two-color photoionization has been used in subsequent research and a loading cross section was roughly estimated [12], the photoionization loading of Yb^+ has not been quantitatively investigated thus far. The purpose of this study is to conduct quantitative measurements of the loading rate of Yb^+ loaded through photoionization. We compare various loading conditions, and discuss the ionization scheme of one-color photoionization and the effect of the charge exchange collision on isotope-selective loading, which have not been clarified so far.

1.2 Purpose of present study and outline of this thesis

In order to conduct quantitative measurement of the loading rate of Yb^+ produced by photoionization, we use the electric resonance detection of the secular motion of the trapped ions. For this purpose, we stored a large number of ions with buffer-gas cooling. In the electric resonance detection method, the excitation of the secular motion of the trapped ions is detected by using a probe radio frequency (RF) field. This method is advantageous for quantitative investigations of the loading rate in two ways: (i) One

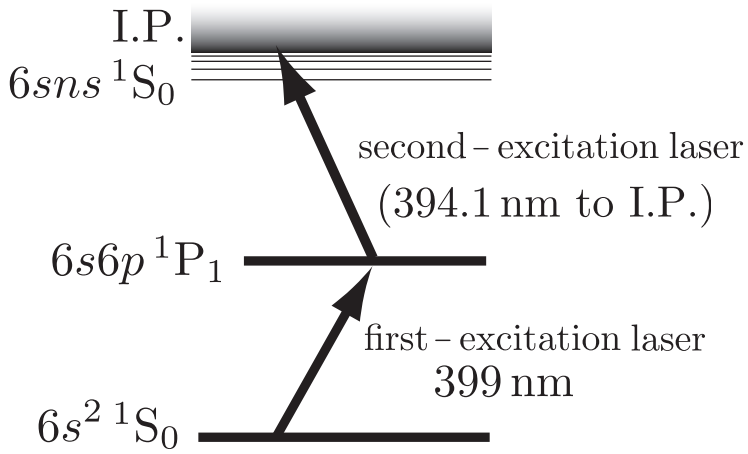

Fig. 1.2 Partial energy level of neutral Yb for photoionization scheme. I.P., ionization potential.

can determine the number of trapped ions from the electric resonance signal [13], which enables us to estimate the loading cross section. In a previous study [14], the electric resonance was used for measurement of electron-impact ionization cross sections of helium in a somewhat different way from ours; in that study, the ion density was estimated from the shift in the secular frequency by the space charge of trapped ions. (ii) No radiation is required for detecting trapped ions. The latter advantage is particularly useful in the case of Yb^+. When Yb^+ is irradiated with resonant light in the presence of buffer gases, Yb^+ is pumped to the $^2F_{7/2}$ metastable state [15, 16] and has a loss in the excited state because of molecular formation with background gases [17]. In ultra high vacuum, these problems are eliminated. However, laser cooling is required to observe trapped Yb^+. The fluorescence intensity is not only proportional to the number of Yb^+ ions but also depends on the translational energy of Yb^+, which is a function of laser detuning and of the total number of trapped ions. Even when the loading rate can be determined from the step increase in the fluorescence caused by one-by-one loading, it may be influenced by the cooling efficiency, which depends on the detuning and intensity of the cooling laser.

We also investigate the charge exchange process between the trapped Yb^+ ions and the Yb atoms from the oven. This is one of the possible causes that limit the number of ions that have been purely isotope-selective loaded [8]. We discuss the effect of the charge exchange collision using the measured rates of loading and charge exchange. Charge exchange cross section or rate coefficients of the collisions between Yb^+ and Yb have been

theoretically estimated in a large energy range [18] and experimentally determined in the semiclassical regime [19]. Measurement of a charge exchange cross section using electric resonance detection was reported in [20].

The following is the outline of this thesis. Before we investigate the photoionization loading of Yb^+ in detail, we improve the number estimation using the electric resonance detection and prepare light sources to be used for photoionization.

Chapter 2

In this chapter, we first describe the principles of the RF trap and the electric resonance detection method. One can determine the number of trapped ions by using the electric resonance signal. The product of the signal height and width is in proportion to the ion number. However, when the trap potential has an anharmonicity, which accompanies the trap ordinarily designed, the signal is distorted and an uncertainty in the number estimation is much increased. We found a method to avoid the problem of the anharmonicity in order to compare the relative loading rate with various conditions. Then, we decrease the uncertainty in the number estimation even in presence of the anharmonicity. This enables us to determine the number loading rate required for estimation of the loading cross section. We shortly describe the collective oscillation of trapped ions. This is used for measurement of the charge exchange rate.

Chapter 3

In this chapter, we describe the light sources that we developed for photoionization of Yb atoms. In order to photoionize Yb atoms, two light sources are required, i.e., one is used for driving the $^1S_0 - {}^1P_1$ transition at 399 nm. the other is for ionizing the Yb atoms in the $^1P_1$ state. A continuous-wave (CW), single-frequency, and continuous frequency-tunable laser is desirable as a light source for driving the $^1S_0 - {}^1P_1$ transition. This enables us to conduct isotope-selective loading by using the isotope shift in the transition. In the course of development of the light sources, we obtain three results that can be widely applied to other systems. First, we found a method to maximize the fundamental enhancement factor of an external cavity, where a nonlinear crystal generating second-harmonics is placed, when a loss by a small residual reflection at anti-reflection coated facet is not negligible small. The external cavity technique is widely used to increase conversion efficiency when one conducts second-harmonic generation (SHG) of a CW laser which is

usually low output power. Second, we found how to realize single-frequency oscillation in an extended-cavity laser diode (ECLD) using a high-power ultra violet diode chip recently developed, even when the diode chip is operated at the maximum output. Third, we found a simple method to detect minor isotope lines in a saturated absorption (SA) spectrum by absorption filtering of major isotope lines. SA is one of the technique used in Doppler-free high-resolution spectroscopy and is applied for the detection of the transitions in atoms and molecules used to obtain reference frequencies.

Chapter 4

This chapter is devoted to describe the results of the main purpose of this thesis described above. We compare the loading rate with various ionization condition, i.e., the dependence of the second-excitation wavelength, the ionization through the Rydberg state, and investigations to clarify the mechanism of one-color photoionization. We measure the loading cross section by using the number of trapped ions estimated from the electric resonance signal by using the improved method described in Chap. 2. We measure charge exchange rate by using enriched ^{171}Yb and ^{174}Yb as a source of Yb atoms. We discuss the effect of the charge exchange collision on isotope-selective photoionization loading.

Chapter 5

We summarize this study with comments for future prospect.

Chapter 2

Principle of RF Ion Traps

In this chapter, we summarize the principle of trapping of charged particles in the RF trap. Then, we describe the method of detecting the trapped charged particles by the electric resonance method. Using the electric resonance signal, one can determine the number of trapped charged particles. In the trap ordinarily designed, the motions of the trapped charged particles have anharmonicity. The anharmonicity distorts the signals and degrades the uncertainty in the number estimation. We develop the number estimation method to be useful even in the presence of anharmonicity. We demonstrate the improved number estimation method with an RF trap used for investigations of photoionization loading. We determine the conversion factor from the relative signal height of the electric resonance signal to the ion number. This conversion factor is required for conversion of the relative loading rate to the number loading rate, from which the loading cross section is estimated. Finally, we briefly describe the collective oscillation, used in the measurement of the charge exchange rate described in Sec. 4.5.

2.1 RF Ion Trap

We use a conventional RF ion trap. The electrodes of the RF trap are composed of two endcap and one ring electrode which surfaces are hyperboraid of revolution as show in Fig. 2.1. An RF driving voltage $V_{\rm ac}\cos\Omega t$ on which a dc electric voltage $V_{\rm dc}$ is superimposed is applied between the endcap and the ring electrodes. The trajectory of a trapped ion is governed by the Mathieu equation: $d^2u_i/d\tau^2 + (a_i - 2q_i\cos 2\tau)u_i = 0$

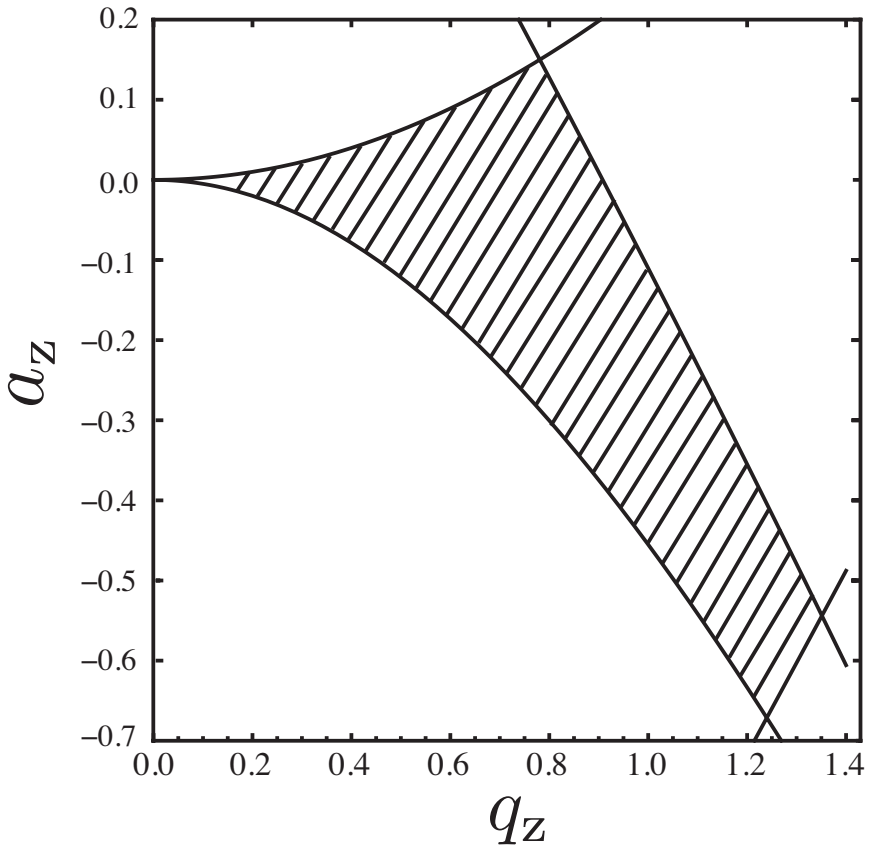

Fig. 2.1 Stability diagram of Mathieu equation. The parameters of a_z and q_z in shaded area satisfy the condition where the charged particle is stably confined in three dimensions.

$(i = r, z)$, where Mathieu parameters a_i and q_i are respectively deduced to be

$$a_z = -2a_r = \frac{-8eV_{\mathrm{dc}}}{mr_0^2\Omega^2} \tag{2.1}$$

and

$$q_z = -2q_r = \frac{4eV_{\mathrm{ac}}}{mr_0^2\Omega^2}, \tag{2.2}$$

where e and m are respectively the charge and mass of the trapped ion. The relationship $r_0^2 = 2z_0^2$ is selected as a conventional trap design, where r_0 is the minimum inner radius of the ring electrode and z_0 is the minimum half distance between the two endcap electrodes. The stability diagram of the Mathieu parameters a_z and q_z are show in Fig. 2.1. The secular frequencies of trapped ions, ω_i, are given by

$$\omega_i = \frac{\beta_i\Omega}{2}, \tag{2.3}$$

where $\beta_i \approx (a_i + q_i^2/2)^{1/2}$. The depthes of the pseudopotential well in the r- and z-direction, $e\overline{D}_r$ and $e\overline{D}_z$ are respectively given by

$$e\overline{D}_r = \frac{m\Omega^2}{8}\beta_r^2 r_0^2 \tag{2.4}$$

and

$$e\overline{D}_z = \frac{m\Omega^2}{8}\beta_z^2 z_0^2 \,. \tag{2.5}$$

2.2 Electric Resonance Detection Method

The secular motion of the trapped ions is excited by a probe RF electric field, when the frequency of the probe is in agreement with the secular frequency. One can determine the absolute or relative number of trapped ions from this resonance signal. The block diagram of the electric resonance detection is shown in Fig. 2.2. The probe RF current source, composed of an RF voltage source with an output of $V_0 \cos\omega t$ and a high resistance $R_{\rm f}$, is connected between the endcap electrodes to excite the secular motion of the trapped ions in the axial- or z-direction. The series resonance circuit resonant at Ω and the parallel resonance circuit resonant at ω are also connected between the endcap electrodes to fix the electrodes to the same electric potential at Ω and DC, respectively. The amplitude at ω between the endcap electrodes is measured using the following electronics composed of a high-input-impedance amplifier, a filter to remove the component at Ω, and a rectifier.

To detect the resonance signal, the probe frequency or the secular frequency of trapped ions are swept. By the probe-frequency sweep, one can determine the absolute number of trapped ions N from the following equation [13]:

$$N = Y_{\rm max}\Delta\omega \left(\frac{4mz_0^2}{\Gamma^2 e^2}\right)\left(\frac{1}{R_f} + G_0\right)\frac{1}{b}\,, \tag{2.6}$$

where the relative signal height $Y_{\rm max}$ is defined as $Y_{\rm max} = (V_{10} - V_1)/V_{10}$; here V_{10} and V_1 are the values of the voltage between the parallel resonance circuit at ω when the ions are removed and trapped, respectively. $\Delta\omega$ is the full width at half maximum of the relative absorption signal in angular frequency, $b = [(2 - 1.5Y_{\rm max})/(2 - 0.5Y_{\rm max})]^{1/2}$, Γ is a compensation factor for the fact that the endcap electrodes are not parallel plates [13],

and G_0 is the conductance of the parallel resonance circuit without trapped ions. The electric resonance detection can be applied to any type of traps in order to estimate N, although a large number of trapped ions, e.g., 10^4 ions in our setup, is required in the case of the trap related to the RF trap. The value of Γ depends on the electrode shape and the ratio between the translational energy of trapped ions and the trap potential [13].

To sweep the secular frequency of trapped ions, the sweep of V_{dc} is widely used because of its convenience. The equation to determine N from the signal detected by the V_{dc}-sweep is not known. However, one can employ the signal obtained by the V_{dc}-sweep for comparing the relative number of trapped ions [21].

2.2.1 Anharmonic oscillation

In the usual trap setup, the signal is distorted by an anharmonicity, which causes a hysteresis and a shift of the resonance frequency. Figure 2.3 shows a sample of the anharmonic electric resonance signal detected with our setup through the probe-frequency

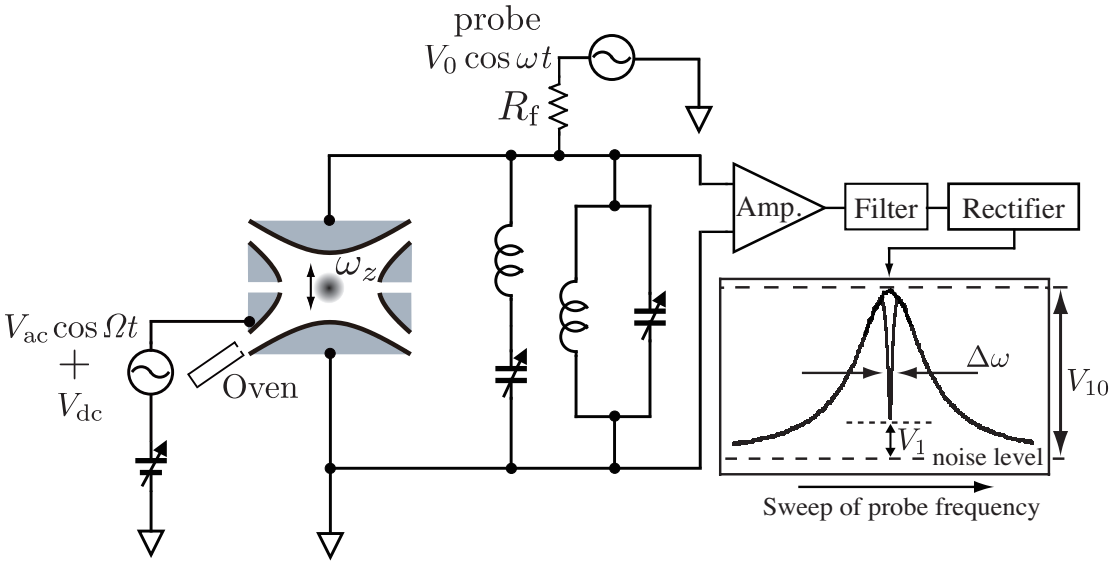

Fig. 2.2 Schematic diagram of the experimental setup for electric resonance detection of trapped ions in radiofrequency (RF) trap. When the secular frequency of trapped ions ω_z equals the probe frequency ω, the trapped ions absorb the probe energy and an absorption signal is observed. The series resonance circuit removes the component at the frequency Ω of the RF driving voltage.

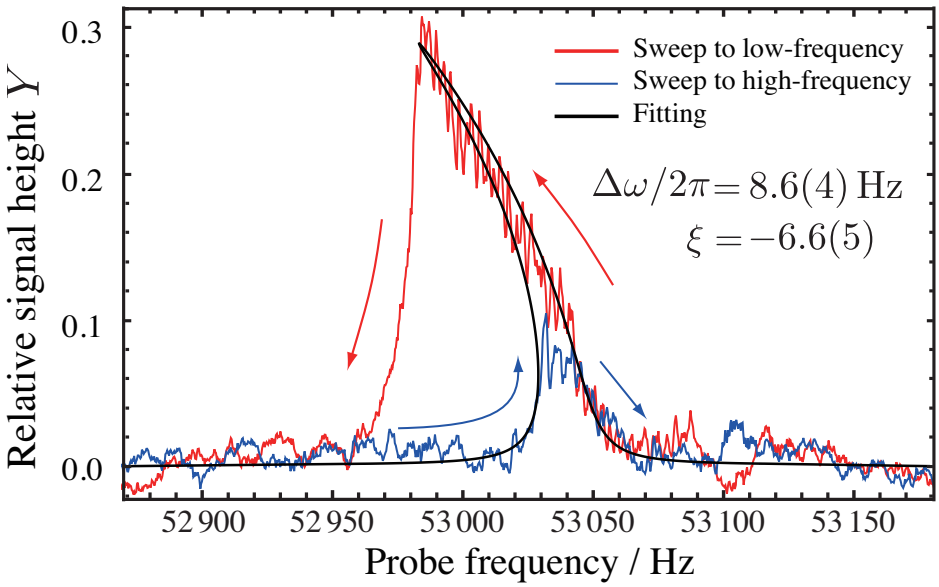

Fig. 2.3 Sample of electric resonance signal with anharmonicity detected by probe-frequency sweep. We show a relative signal height Y, i.e., difference in the parallel resonance curve in the cases with and without trapped ions. The arrows indicate the scanning directions of the probe frequency. The parameters of the electric resonance detection are given in Sec. 2.2.1. The solid line denotes a fitting curve expressed by Eq. (2.7). The best fitting values of $\Delta\omega$ and ξ are shown in the figure.

sweep with two sweep directions, i.e., from low to high frequency and its reverse direction. The anharmonicity is caused by the fact that the electrodes are not infinitely extended hyperboloids of revolution [22] and is modified by the space charge of trapped ions when the number of trapped ions is large [23]. When the trap electrodes are symmetric along the trap axis and the plane at $z = 0$, the truncated trap electrode generates an octupole potential that induces the anharmonicity. The axial or radial secular frequency is proportional to the square of the amplitude of the secular motion, which is expressed by a Duffing equation. Even when the signal has this anharmonicity, the signal height detected by the sweep direction of the larger signal is the same as that in the case of no anharmonicity [22]. In the case of no anharmonicity, increase in the signal height grows smaller as the number of trapped ions increases, while the product of the signal height and width still proportionally increases as shown in Eq. (2.6). However, when the number of trapped ions is small and $Y_{\max}$ is smaller than 0.2, $Y_{\max}$ is proportional to the number of trapped ions. Even when $Y_{\max}$ is 0.3, a deviation from the proportional increase to the

ion number is approximately 10%. This is proved by comparison between $Y_{\max}$ and the product of $Y_{\max}$ and $\Delta\omega$, performed by numerical calculation, irrespective of the probe frequency sweep or $V_{\rm dc}$ sweep [13, 21, 24]. Therefore, when $Y_{\max}$ is smaller than 0.3, it is possible to compare the relative number of trapped ions using only $Y_{\max}$ detected by the sweep direction of the larger signal even in the presence of the anharmonicity. This characteristic enables us to determine the relative loading rate by using $Y_{\max}$, because the relative loading rate is estimated at the start of loading where the number of ions is approximately zero, as we later describe in Sec. 4.1.

If we can measure the conversion factor from the $Y_{\max}$ detected by $V_{\rm dc}$ sweep to N even in the presence of anharmonicity, we will be able to convert the relative loading rate to the number loading rate, from which we can estimate the loading cross section. In the case of no anharmonicity, the measurement of the conversion factor is easily accomplished by detecting the signals to the same number of ions both by the $V_{\rm dc}$-sweep and the probe-frequency sweep. We determine N from the signal by the probe-frequency sweep by using Eq. (2.6), and thus obtain the conversion factor $N/Y_{\max}$. However, when an anharmonicity is present, the signal width of the sweep direction of the larger signal is wider than $\Delta\omega$. Therefore, we need to estimate the value of $\Delta\omega$ from the anharmonic signal in order to determine N using Eq. (2.6).

With the above mentioned anharmonicity, the secular frequency varies in proportion to the square of the amplitude of the secular motion [22]. In the electric resonance signal, the current induced by the secular motion can be detected. The amplitude of the signal is proportional to the velocity and, hence, to the amplitude of the secular motion. Therefore, the shift of the secular frequency can be described to be in proportion to the square of the relative signal height Y of the electric resonance signal, i.e., $\omega_z(Y) = (1+\alpha Y^2)\omega_{z_0}$, as we introduce a factor of proportionality α, where ω_{z_0} is the secular frequency in the absence of anharmonicity. The shape of the electric resonance signal by the probe-frequency sweep can be approximately expressed as a Lorentz profile in the case of no anharmonicity because the quality factor of the signal is high. Subsequently, we approximate the profile of the anharmonic signal by introducing the dependence on the square of the signal amplitude to the secular frequency;

$$\frac{Y}{Y_{\max}} = \left[1 + 4\left(\frac{\omega - \omega_{z_0}}{\Delta\omega} - \xi\frac{Y^2}{Y_{\max}^2}\right)^2\right]^{-1}, \tag{2.7}$$

where ξ is a dimensionless parameter introduced to express the dependence of ω_z on the square of the signal amplitude. The relation between α and ξ is shown as $\xi = \alpha(\omega_{z_0}/\Delta\omega)Y_{\max}^2$. By fitting the electric resonance signals detected by the two sweep directions to Eq. (2.7), we estimate the value of $\Delta\omega$ and then determine N from Eq. (2.6) even in presence of the anharmonicity.

We demonstrate the improved number estimation method using an RF ion trap used for investigations of photoionization loading, and determined the conversion factor $N/Y_{\max}$.

2.2.2 Experimental setup

The ion trap used has r_0 of 17.0 mm and z_0 of 12.0 mm. The AC driving voltage has an amplitude of $V_{\rm ac} = 250\,\mathrm{V}$ and a frequency of $\Omega/2\pi = 300\,\mathrm{kHz}$. The axial secular frequency of trapped $^{174}\mathrm{Yb}^+$, $\omega_z/2\pi$, is approximately 53 kHz. The trap potential in z- and r-direction are 15 eV and 11 eV, respectively, calculated from Eqs. (2.4) and (2.5). One of the endcap electrodes is made of a mesh. The ring electrode has four holes in the $z = 0$ plain, arranged at 90 degrees to each other. These allow us to introduce laser beams. Two ovens are used for producing Yb vapor; one oven contains an enriched isotope ^{174}Yb while the other contains ^{171}Yb. The abundances of the enriched 174 and 171 sources are 98.97% and 90.6%, respectively. We use the ^{174}Yb oven except that we notify the use of ^{171}Yb oven. The background pressure of the vacuum chamber where the ion trap apparatus is placed is $3 \times 10^{-7}\,\mathrm{Pa}$. We introduce helium gas having a pressure of $5.3 \times 10^{-5}\,\mathrm{Pa}$ as a buffer gas for cooling of trapped ions. The lifetime of trapped $^{174}\mathrm{Yb}^+$ ions is over $10^4\,\mathrm{s}$.

The parameters of the electric resonance detection are as follows: $V_0 = 3\,\mathrm{mV}$, $R_{\rm f} = 2\,\mathrm{M\Omega}$, and $G_0 = 3 \times 10^{-7}\,\mathrm{S}$. Because the translational energy of the buffer gas cooled Yb^+ ions, which is supposed to be approximately 1200 K [25], is much smaller than the trap potential and the ions are located around the center of the trap, Γ is approximately 1 [13]. The sweep rate of $V_{\rm dc}$ and probe frequency $\omega/2\pi$ are set to be 50 mV/s and 50 Hz/s, respectively. These are sufficiently slow in order to prevent ringing of the signal [24].

2.2.3 Results

We determine the conversion factor $N/Y_{\max}$, as described in Sec. 2.2, for $Y_{\max} \leq 0.3$. For the sample shown in Fig. 2.3, we determine $\Delta\omega/2\pi$ and ξ to be 8.6(4) Hz and $-6.6(5)$,

respectively, by fitting Eq. (2.7) to the signals for probe-frequency sweep in two directions. Accordingly, we estimate $N/Y_{\max}$ for eight samples between $Y_{\max} = 0.1$ and 0.3 as shown in Fig.2.4, and average these values to determine $N/Y_{\max}$ to be $2.7(3) \times 10^5$. The uncertainty is caused by the fitting error and the small deviation of $Y_{\max}$ from the proportional increase to N as described in Sec. 2.2.1.

2.3 Collective oscillation

When the ions having similar, but not the same, charge-to-mass ratios are simultaneously trapped, a collective oscillation is observed, i.e., the ion cloud moves as one particle [26]. This results in a single resonance in the electric resonance signal; the resonance frequency depends on the ratio of the number of each ion. In the case of two singly charged ion species, the resonance frequency corresponds to that of the equivalent mass $m_0 = [(N_1m_1 + N_2m_2)m_1m_2/(N_1m_2 + N_2m_1)]^{1/2}$ [27]. One can estimate the ratio of the two ion species from the resonance frequency. If we prepare two pure isotopes of atoms,

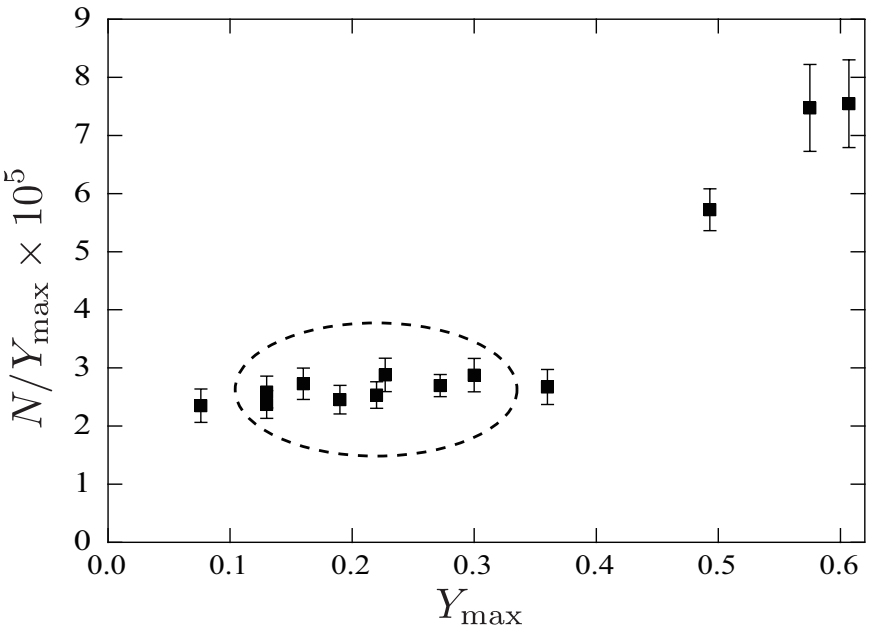

Fig. 2.4 Dependence of conversion factor $N/Y_{\max}$ on $Y_{\max}$. Since the number of trapped ions N is proportional to $Y_{\max}$ when $Y_{\max} \leq 0.3$, $N/Y_{\max}$ is approximately constant. We determine $N/Y_{\max}$ from eight samples as indicated by dotted line circle, which is used for estimation of the loading cross section.

trap the ions of one of the two isotopes, and collide them with the other isotope of atoms, we can determine the charge exchange rate from a temporal change in the resonance frequency. We will describe the measurement of the charge exchange rate between Yb^+ and Yb atoms in Sec. 4.5.

2.4 Summary

In this chapter, we summarize the principles of the techniques used in this work, i.e., the RF trap and the electric resonance detection. In the electric resonance detection, one detects the frequency of the secular motion of trapped ions. We focus on two characteristics of the secular motion; one is the anharmonic oscillation, the other is the collective oscillation. The anharmonicity accompanies the trap ordinarily designed, and degrades the uncertainty in estimation of the number of trapped ions using the electric resonance signal. We develop the number estimation method in order to improve the uncertainty even in the presence of anharmonicity. We determine the conversion factor $N/Y_{\max}$ with an uncertainty of 10% when $Y_{\max} \leq 0.3$. This enables us to convert to the $Y_{\max}$ loading rate to the number loading rate used for determination of the loading cross section.

The collective oscillation is used for measurement of the ratio of the isotopes of trapped ions. We will apply this to the measurement of the charge exchange rate as described in Sec 4.5.

Chapter 3

Light Sources for Photoionization of Yb

In this chapter, we describe the light sources for ionizing Yb atoms. As we describe in Chap. 1, the photoionization scheme that we mainly investigate is the two-color excitation, where the $^1S_0 - {}^1P_1$ transition in Yb atoms at 399 nm is driven as the first-excitation and Yb atoms in the $^1P_1$ state are ionized by the second-excitation laser. For the investigations, we need a light source at 399 nm and another one for ionizing Yb atoms in the $^1P_1$ state.

For the light source at 399 nm, a single-frequency continuous-wave (CW) tunable light source is desirable because this enables us to conduct isotope-selective loading by using the isotope shifts in the $^1S_0 - {}^1P_1$ transitions. We develop two light sources which satisfy the requirement. One is a frequency-doubled titanium-sapphire laser (Ti:S) and the other is an extended cavity laser diode (ECLD).

The conversion efficiency of the second-harmonic generation (SHG) of CW radiation in a nonlinear crystal is usually small. In order to enhance it, the nonlinear crystal is placed in an external cavity. We find a problem when we maximize the enhancement factor, and demonstrate a solution to it, as shown in Sec. 3.2. Recently, diode lasers in the ultraviolet region are available. We can realize a compact tunable single-frequency light source by constructing an ECLD using one of those diode chips. We develop an ECLD at 399 nm using a high-output power diode chip which is very recently available. We describe the development in detail in Sec. 3.3 because the performance of the ECLD composed of a high-output power ultraviolet diode chip is not known. We also use other three ECLDs with low-power ultraviolet diode chips of different center wavelengths for the second excitation laser, although they are out of the scope of this thesis.

After we prepare the light sources, we next need to conduct frequency tuning of them. For the light source at 399 nm, a precise tuning is required for isotope-selective loading. Saturated absorption (SA) is one of the techniques used in high-resolution spectroscopy and is applied for the detection of the transitions in atoms and molecules used to obtain reference frequencies. Even after employing SA, isotope shifts and hyperfine structures are sometimes incompletely resolved, and these unresolved lines contain signals of target isotopes required for subsequent investigations. We demonstrate a simple method to detect minor isotope lines in SA by absorption filtering of major isotope lines. We investigate this method for the spectroscopy of the $^1S_0 - {}^1P_1$ transition in Yb at 399 nm by controlling the density of Yb atoms by varying the discharge current of a hollow cathode lamp.

3.1 Second Harmonic Generation of Titanium Sapphire Laser with External Cavity Technique

The light source for driving the $^1S_0$ - $^1P_1$ transition at 399 nm, which we first developed, is a frequency-doubled Ti:S laser. In order to generate CW ultraviolet light, SHG in nonlinear crystals has long been used. To increase the SH power, a nonlinear crystal is placed in an external cavity to enhance the fundamental power because of the low power of the beam from the CW laser [28]. Brewster-cut crystals [29,30] or antireflection (AR)-coated normal-cut crystals [31] are used as a nonlinear crystal in the external cavity. The former has the advantages that no loss is imposed by surface reflection and that the astigmatism and coma introduced at the Brewster-cut facets are compensated by the folding angle of the concave mirrors to focus the beam in the crystal [32]. The latter is also widely used because it is easier to align the ring cavity and the aberrations are small provided the folding angle is small.

When the finesse of an external cavity is sufficiently high to obtain a large fundamental enhancement factor, the enhancement factor, as described in the following section, is greatly affected by the round-trip loss. The small residual reflection at the crystal facets is one of the main causes of this loss when a normal-cut crystal is used, even though the crystal facets are AR-coated. The reflected beams from the two facets of the normal-cut crystal are subjected to interference, i.e., the crystal acts as an intracavity etalon. This

shows that the loss imposed by the residual reflection at the crystal facets is eliminated when the reflected beams at the two facets are subjected to constructive interference. This technique is based on the theory of coupled cavity. Simultaneously, the interference causes the wavelength dependence of the enhancement factor, and the enhancement factor changes over long-time or day-to-day operation.

In this section, we discuss the effect of the small residual reflection at the crystal facets on the enhancement factor and the wavelength dependence on the enhancement factor. To achieve constructive interference, i.e., the maximum enhancement factor at any wavelength, we demonstrate that temperature tuning is effective in our system containing a normal-cut β-BaB_2O_4 (BBO) crystal as a nonlinear crystal in an external cavity.

3.1.1 Effect of round-trip loss on enhancement factor

The fundamental enhancement factor A is described by

$$A = \frac{1-R}{(1-\sqrt{RV})^2}\,, \tag{3.1}$$

where R is the input mirror reflectivity and the loss factor V is defined as $V = 1 - L$, where L is the fraction of the round-trip loss [28]. The linewidth of the fundamental laser is assumed to be narrower than the resonance width of the external cavity. Figure 3.1 shows the enhancement factor A as a function of the input mirror reflectivity for various values of V. When the impedance matching condition, i.e., $R = V$, is satisfied, the maximum enhancement factor $A_{\max} = 1/(1-R)$ is achieved. Figure 3.2 depicts the Eq. (3.1) to clarify the dependence of the enhancement factor A on V with the reflectivity of the input mirror R as a parameter. When R is high, a small difference in the intracavity loss markedly changes the enhancement factor. For example, for an external cavity with an input mirror of $R = 0.99$ and a fraction of round-trip loss of $L = 0.008$, one obtains $A = 125$. An increase in L of only 0.002, i.e., to 0.01, results in a decrease in A to 100. On the other hand, when $R = 0.95$, an increase in L of 0.002 only decreases A from 59 to 55. In addition, the SH power is proportional to the square of the enhancement factor. To achieve a high SH power by realizing a high enhancement factor using a high-reflectivity input mirror, it is therefore essential to minimize the loss in the external cavity.

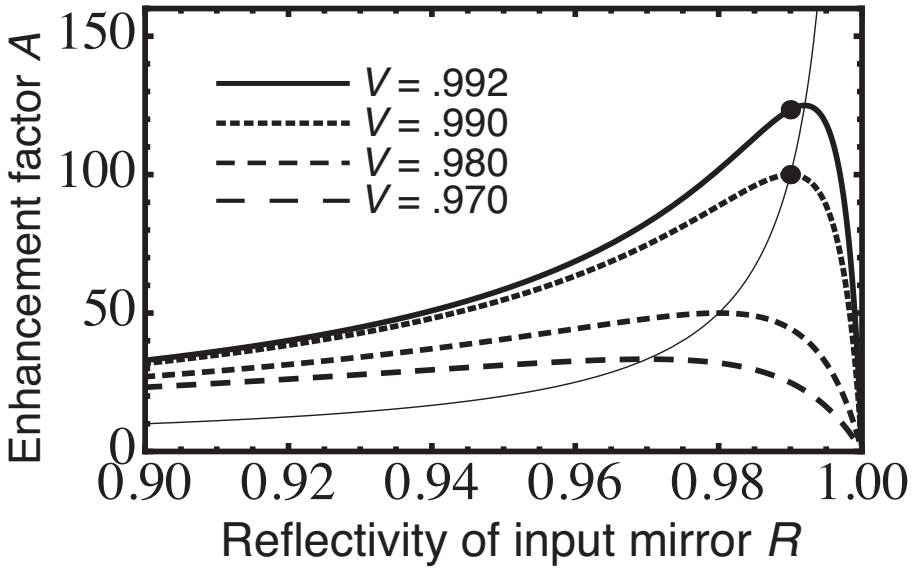

Fig. 3.1 Calculated enhancement factor A as a function of the input mirror reflectivity R with the loss factor V as a parameter, where $V = 1 - L$ as L is the fraction of the round-trip loss. When the impedance matching condition, i.e., $R = V$ is satisfied, A is maximized for a given value of V. The thin line shows the maximum enhancement factor as a function of R. The two dots indicate the maximum and the minimum enhancement factor observed in our setup.

Effect of AR-coated facets of normal-cut nonlinear crystal

When one uses an AR-coated normal-cut nonlinear crystal in the external cavity, the residual reflection at the crystal facets is one possible loss factor. However, it is possible to eliminate the loss imposed by the residual reflection when the reflected beams from the two facets are subjected to constructive interference, i.e., the intracavity etalon composed of the residual reflection at the two crystal facets is resonant. The longitudinal mode spacing or free spectral range of a Fabry-Perot cavity in terms of wavelength $\Delta\lambda$ is given by

$$|\Delta\lambda| = \frac{\lambda^2}{2nl}\,, \tag{3.2}$$

where λ is the wavelength in vacuum, l is the distance between mirrors, and n is the refractive index of the material. We estimate $\Delta\lambda$ in our setup (see Sec. 3.1.2), which contains a 10-mm-long BBO crystal, to be 0.019 nm for a fundamental wavelength of $\lambda = 798$ nm, where $n = 1.66$ for ordinary light at 798 nm obtained from Sellmeier's

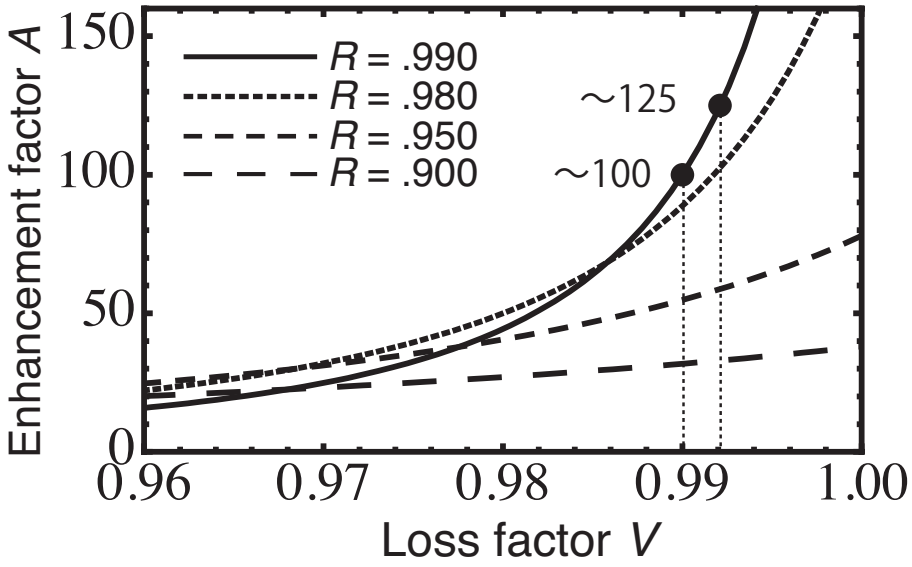

Fig. 3.2 Calculated enhancement factor A as a function of the loss factor V defined as $V = 1 - L$, where L is the fraction of the round-trip loss. When the reflectivity of the input mirror R is high (> 0.98), the enhancement factor is strongly affected by the round-trip loss. For example, for $R = 0.990$, A decreases from 125 to 100 when L increases only by 0.002 from 0.008 to 0.010.

equations described in Appendix A [33]. This shows that the enhancement factor, and hence the SH power, depends on the fundamental wavelength.

It is desirable to achieve the maximum enhancement factor at any wavelength. For this purpose, the interference caused by the residual reflection at the two crystal facets must be tuned constructively. We investigate the temperature tuning of the optical path length of the cavity formed between the facets of the BBO crystal. In the worst case, temperature tuning is required to change the destructive interference to constructive interference. To realize this, the optical path length in the crystal is tuned by a quarter wavelength, with the change of the crystal temperature ΔT given by

$$\frac{d(nl)}{dT}\Delta T = (n\frac{dl}{dT} + l\frac{dn}{dT})\Delta T = \frac{\lambda}{4}\,, \tag{3.3}$$

where T is the temperature of the crystal. We estimate ΔT for our BBO system. The thermo-optic coefficient dn/dT for ordinary light is -16.6×10^{-6}/K [34]. The thermal expansion coefficient, $(1/l)dl/dT = 28 \times 10^{-6}$/K at $\theta = 29.3°$ of the phase-matching angle of our target wavelength of 798 nm, is derived from the equation $\alpha_a \sin^2\theta + \alpha_c \cos^2\theta$ [35]

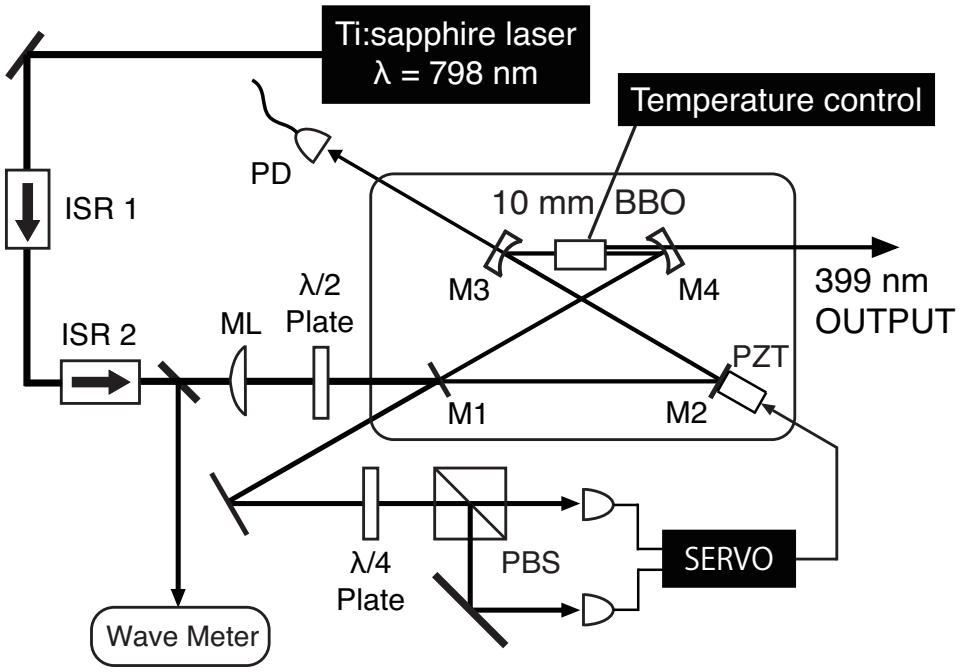

Fig. 3.3 Experimental setup. ISR, isolator; ML, mode-matching lens ($f = 750$ mm); M3, M4, concave mirrors with curvature radius of 50 mm; PZT, piezotransducer; PBS, polarizing beam splitter; PD, photodiode. The PD is used to monitor the fundamental power inside the external cavity.

and the known values of α_a and α_c of 4×10^{-6}/K and 36×10^{-6}/K, respectively [34]. We find that a temperature change of 0.7 K is required to change the optical path length by $\lambda/4$, i.e., to tune the enhancement factor from the minimum to the maximum. The temperature tuning of a BBO crystal in an external cavity has also been applied to tune the resonance frequency of the external cavity to enable frequency scanning of a laser system [36].

3.1.2 Experimental setup

Figure 3.3 shows a schematic diagram of the experimental setup. Radiation with a wavelength of 798 nm from a single-frequency CW titanium sapphire laser (Schwartz Electro-Optics Inc., Titan-CW). Two galvoplates and a galvo-driven thin etalon synchronously rotated with the galvoplates are introduced by us to enable frequency scanning.) is frequency doubled using a BBO crystal in an external cavity. The external cavity

is composed of four mirrors in a bow-tie configuration. The total cavity length is approximately 400 mm, corresponding to a free spectral range of 750 MHz. The reflectivity of the input mirror R_{M1} is 0.990 ± 0.002, and those of the other mirrors R_{M2}, R_{M3}, and R_{M4} are more than 0.998 for the fundamental wavelength of 798 nm. The transmissivity of the output mirror M4 is 0.95 at 399 nm. To focus the fundamental beam in the BBO crystal, we use two concave mirrors with a curvature of 50 mm. The resonance frequency of the external cavity is locked to the frequency of the laser by controlling the cavity length using a piezotransducer (PZT) on which M2 is mounted. The frequency deviation from the cavity resonance is detected by a polarization spectroscopic method [37].

The BBO crystal is cut to $\theta = 29.3°$ to achieve Type-I phase matching to the normal incidence of the fundamental beam at 798 nm (Appendix A). The length of the crystal is 10 mm. The azimuth angle is cut to $\phi = 0°$ to maximize the nonlinear coefficient. The input and output facets are AR-coated for both fundamental and SH wavelengths. The BBO crystal is placed in a holder made of copper, which is mounted on a Peltier element. The temperature of the copper holder, measured using a thermistor, is temperature-controlled with a stability better than 0.01°C (Thorlabs Inc., TED200C). Owing to the high finesse of the external cavity, a beam reversely propagating in the cavity is built up and fed back to the laser. This prevents electronic locking of the cavity resonance to the laser frequency. To avoid optical feedback, we inserted two isolators (Isowave, I-80T-5M) with isolation above 35 dB.

3.1.3 Results and analysis

We measured the fundamental power built up in the external cavity and the SH power as a function of the fundamental wavelength, as shown in Fig. 3.4. We observed interference fringes in the fundamental power, and the SH power synchronously changed in proportional to the square of the fundamental power. The pitch of the fringes was measured to be 0.019 nm. This value was in agreement with that obtained in Sec. 3.1.1. Therefore, we conclude that the fringes observed in Fig. 3.4 are caused by the residual reflection at the two facets of the BBO crystal.

We estimated the enhancement factor A by measuring the finesse of the external cavity. The finesse $\mathcal{F}$ is determined from the input mirror reflectivity R and the round-trip loss

factor V by the following equation:

$$\mathcal{F} = \frac{\pi(RV)^{1/4}}{1-\sqrt{RV}}. \tag{3.4}$$

One can determine the value of $\sqrt{RV}$, and then V, from the finesse $\mathcal{F}$. Then, the enhancement factor A can be estimated from Eq. (3.1). We measured the finesse by linearly scanning the frequency of the Ti:S laser by rotating the galvoplates inside the laser cavity. The finesse was determined to be 350 for the constructive interference and 310 for the destructive interference. From the reflectivity of the input mirror, $R_{M1} = 0.990 \pm 0.002$, the corresponding enhancement factors A was estimated to be 125 ± 25 and $100, \pm 20$, and the ratios of the round trip loss L to be $0.008, \pm 0.002$ and $0.010, \pm 0.002$, respectively. The change in L shows that the residual reflectivity at the AR-coated crystal facet is approximately 0.001 for each facet.

Figure 3.5 shows the fundamental and SH powers measured by changing the crystal temperature. We again observed the same periodic change in the enhancement factor as that shown as a function of the wavelength in Fig. 3.4. The net optical path length nl in the crystal changed with its temperature and a temperature tuning of 3 K was required

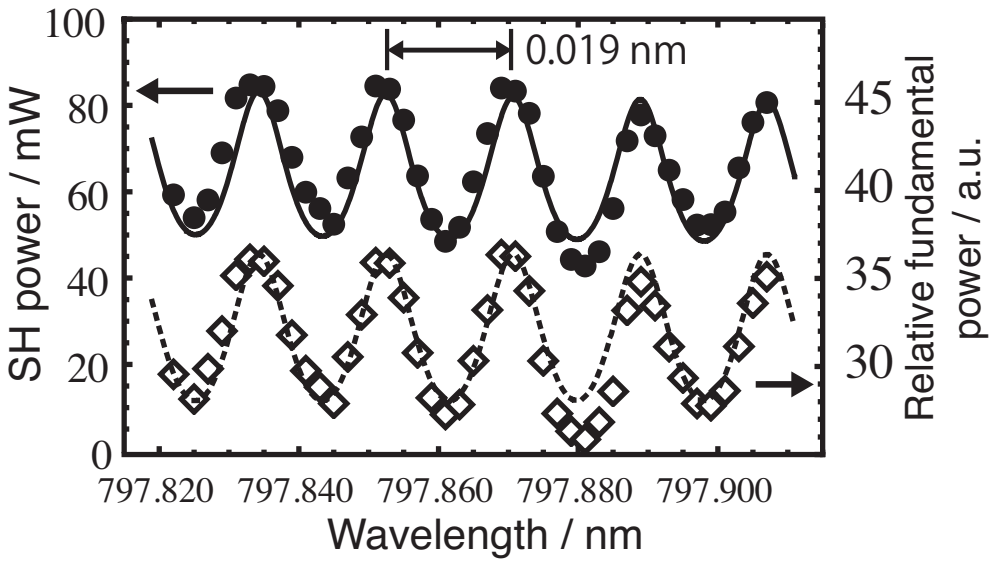

Fig. 3.4 Dependence of SH power (solid circles) and fundamental power (open diamonds) on the fundamental wavelength. The dashed curve is a Fabry-Perot function fitted to fundamental power. The solid curve is the square of the Fabry-Perot function fitted to SH power.

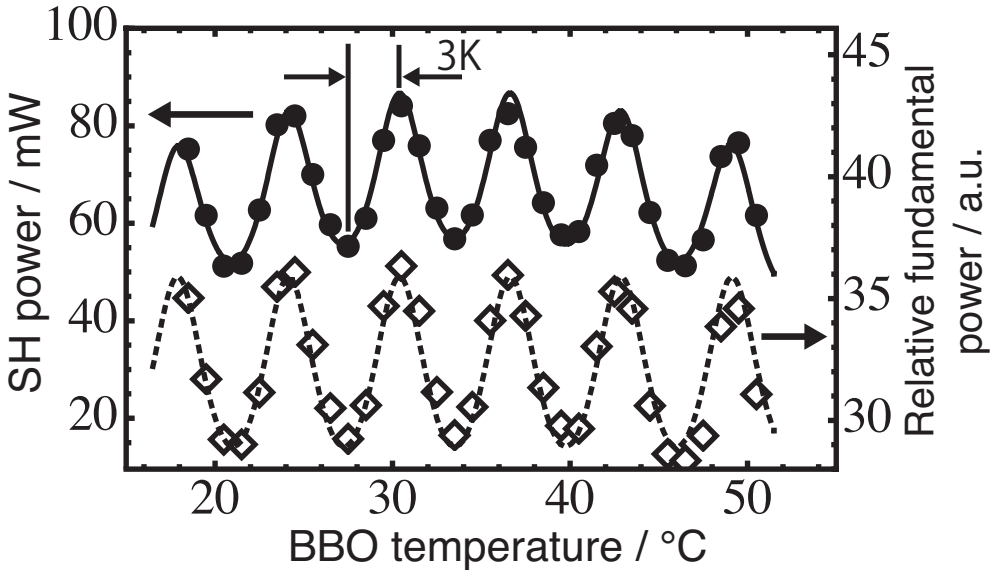

Fig. 3.5 Dependence of SH power (solid circles) and fundamental power (open diamonds) on temperature of BBO crystal. The dashed curve is a Fabry-Perot function fitted to the fundamental power. The solid curve is the square of the Fabry-Perot function fitted to the SH power. The decrease due to phase-mismatching expressed as the square of the sinc function is also included in the fitting.

to change the destructive interference to constructive interference, or a half cycle of the interference fringe in Fig. 3.5. This result is different from the theoretical estimation of 0.7 K obtained in Sec. 3.1.1. The reason for the discrepancy is not yet known. Assuming that the thermooptic coefficient is correct, we estimate the value of $(1/l)dl/dT$ at 29.3° to be 14×10^{-6}/K.

When temperature-tuning the interference fringe, it is important that the phase-mismatching tolerance in SHG is much larger than the tuning temperature for each half cycle of the fringe. We define the phase-mismatching tolerance as the full width at half maximum (FWHM) of a sinc function $[\sin(\Delta kl/2)/(\Delta kl/2)]^2$, where Δk represents the phase mismatch. From the known parameters, we calculate the phase-mismatching tolerance to be 4.8 K as the estimation conducted in [34]. However, Fig. 3.5 shows that the effect of the phase-mismatching tolerance was negligible for tuning of 3 K. The observed phase-mismatching tolerance of approximately 50 K was much larger than the estimated value of 4.8 K. The discrepancy is caused by the fact that the interaction length is shorter than the crystal length owing to the double refraction in the BBO crystal [23].

The interaction length, i.e., the aperture length, expressed as $l_a = \pi^{1/2}\omega_0/\rho$ [38], was calculated to be 0.6 mm in our case, where ρ is the walk-off angle as described below and in Appendix A. The FWHM phase-mismatching tolerance, derived using l_a instead of l, is 80 K. This is close to the experimental result.

We measured the day-to-day reproducibility of the SH power at a fixed wavelength for one week; we switched the setup on and off every day but the crystal temperature was continuously controlled for one week. A fluctuation of the SH power of 10 % was detected, while 40 % fluctuation was observed in the day-to-day operation without temperature control owing to the fluctuation of the ambient room temperature within approximately 2 °C.

When we tune the optical path length in the crystal to produce constructive interference, the reflection at the crystal facets is eliminated. Therefore, the backward beams in the external cavity, and hence the optical feedback to the laser, are minimized. We achieved electronic locking of the cavity resonance to the laser frequency using only one isolator because of the reduced optical feedback. When we changed the crystal temperature by 0.7 K from that resulting in constructive interference, we found that a second isolator was necessary for stable frequency locking. Each isolator has an insertion loss of 11 %. Therefore, the removal of one isolator has the benefit of increasing the fundamental power and hence the SH power.

The method of temperature tuning to maximize the enhancement factor can be applied to an external cavity with other materials used as a nonlinear crystal. For example, with a 10 mm long normal-cut LBO crystal for SHG at 798 nm, we estimate that a temperature change of at most 0.3 K could maximize the enhancement factor according to our calculation for the BBO crystal. A different tuning method such as electronic tuning using an electrooptic effect may also be feasible.

SH power and conversion efficiency

The SH power generated under constructive interference is plotted in Fig. 3.6 as a function of the fundamental power. When the fundamental power in the crystal is depleted by conversion to the SH power and the absorption of the fundamental power and SH power in the crystal is negligible, the total conversion efficiency $\gamma_{\text{total}} = P_{2\omega}/P_{\omega}^2$, where P_ω and

$P_{2\omega}$ are fundamental power and SH power, respectively, is expressed as

$$\begin{aligned}\gamma_{\text{total}} &= \gamma_{\text{SHG}}\gamma_{\text{mm}}^2 A^2 \\ &= \gamma_{\text{mm}}^2 A^2 \frac{16\pi^2}{\epsilon_0 c\lambda_\omega^3}\frac{d_{\text{eff}}^2\, l}{n^2} h(B,\xi)\,, \end{aligned} \tag{3.5}$$

where γ_{SHG} is the single-path conversion efficiency; γ_{mm} is the coupling or mode-matching efficiency of the fundamental beam to the external cavity; d_{eff} is the effective nonlinear coefficient; ϵ_0 is the electric constant; c is the vacuum speed of light; λ_ω is the fundamental wavelength in vacuum; n is the refractive index, which is the same for the fundamental and SH powers upon phase matching; $h(B,\xi)$ is the focusing function introduced by Boyd and Kleinman [38], where B is the double-refraction parameter defined as $B = \rho(k_\omega l)^{1/2}/2$, where ρ is the walk-off angle and k_ω is the propagation constant at the fundamental wavelength in the crystal; and ξ is the focusing parameter defined as $\xi = l/b$, where $b = w_0^2 k_\omega$ is the confocal parameter and w_0 is the radius of the fundamental beam at focus.

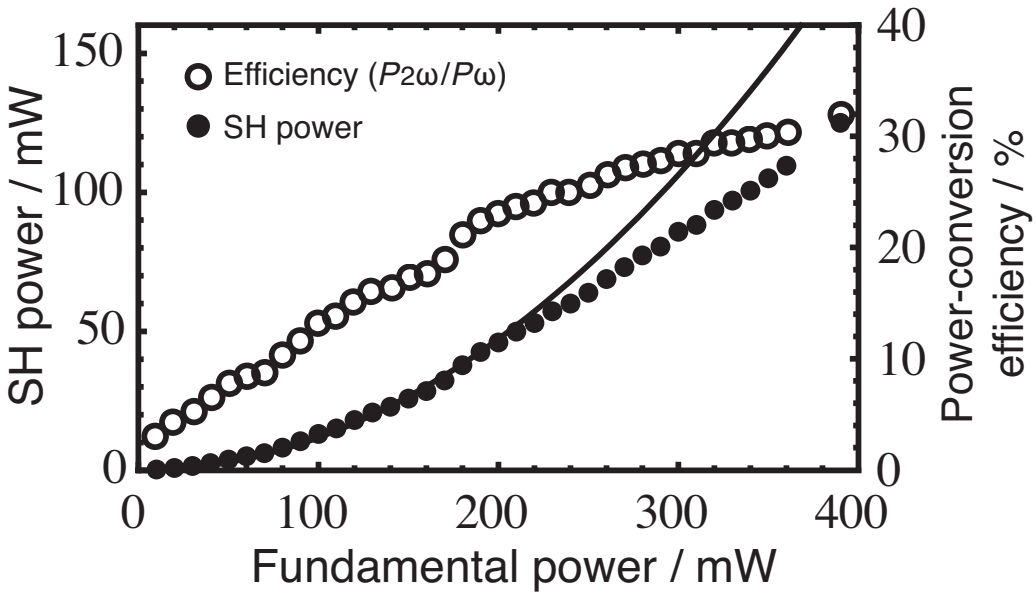

Fig. 3.6 SH power and corresponding power-conversion efficiency $P_{2\omega}/P_\omega$ as a function of the fundamental power when the fundamental enhancement factor is maximized by temperature tuning, where P_ω and $P_{2\omega}$ are the fundamental and SH powers, respectively. The solid curve represents the calculated SH power assuming no depletion of the fundamental power by conversion to the SH power. The highest SH power of 125 mW was achieved at a fundamental power of 390 mW.

Our external cavity is designed so that $\xi = 1.39$. The walk-off angle ρ of 68 mrad (or 3.9°) as described in Appendix A, leads to $B = 12$. Then, we estimate the value of h to be 0.058. We calculate d_{eff} to be 1.9 pm/V from the equation $d_{\text{eff}} = d_{31}\sin(\theta+\rho)+d_{22}\cos(\theta+\rho)$ and the known values of the coefficients d_{31} and d_{22} of 0.04 pm/V and 2.3 pm/V, respectively [39]. We estimate γ_{SHG} to be 0.93×10^{-4}/W. We experimentally determined the value of γ_{mm} to be 0.9. Finally, when we assume $R_{\text{M1}} = 0.990$, i.e., $A = 125$ for the constructive interference, we estimate γ_{total} to be 1.2/W. This value is in good agreement with the results shown in Fig. 3.6 in the region of low power-conversion efficiency ($P_{2\omega}/P_{\omega}$) of below 15 %. The conversion efficiency is similar to that obtained using a Brewster-cut BBO crystal [29, 30]. The discrepancy compared with the estimated conversion efficiency in the high power-conversion efficiency region of over 15 % is caused by the depletion of the fundamental power by conversion to the SH power [40].

3.2 External Cavity Laser Diode

In order to realize a more compact and simple light source than the frequency-doubled Ti:S laser, we construct an ECLD with a high-power ultraviolet diode chip having a maximum output power of 100 mW (Nichia, 8C18KS). A diffraction grating having 2400 grooves/mm and a blaze wavelength of 250 nm is placed in a Littrow configuration. The first-order diffracted beam whose power is 25% of the incident power is fed back to the chip, and the zeroth-order reflection whose power is 64% of the incident power is produced as the output. The maximum power with which we achieve a single-frequency oscillation increases as the cavity length of the ECLD is shortened, as shown in Fig. 3.7. At the shortest cavity length of 14 mm, we obtain a tuning range with a single-frequency oscillation of 2 nm as shown in Fig. 3.8 and with a linewidth below 2 MHz and 20 MHz for observation times of below 1 ms and 10 ms, respectively, as shown in Fig. 3.9. The linewidth is measured by beat signals at the frequency of the second harmonic of a titanium sapphire laser. The continuous frequency-tuning range of 3 GHz is achieved by scanning the voltage applied to a PZT which controls the cavity length.

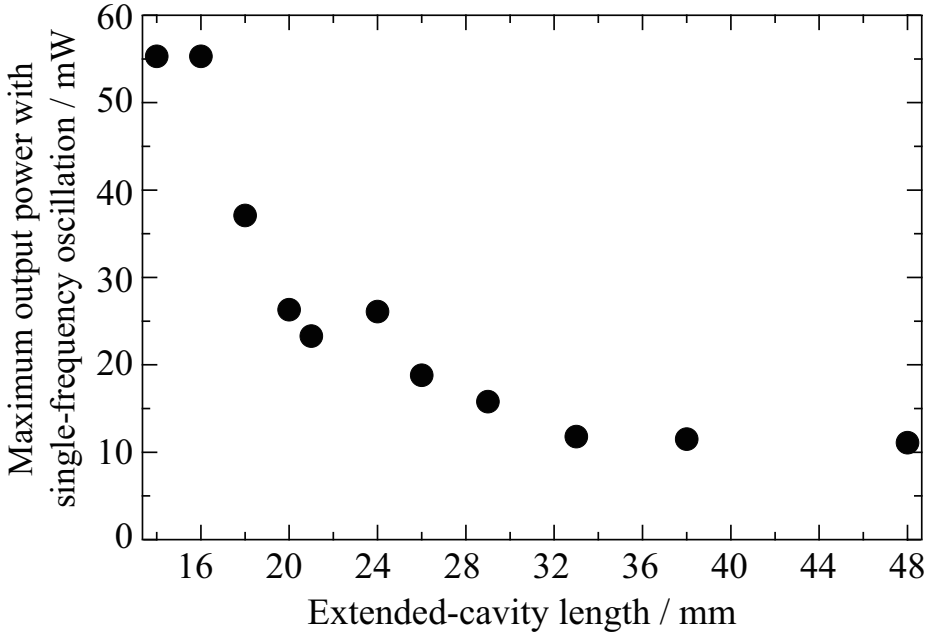

Fig. 3.7 Maximum output power achieved with single-frequency oscillation in ECLD with ultraviolet diode chip as a function of extended-cavity length.

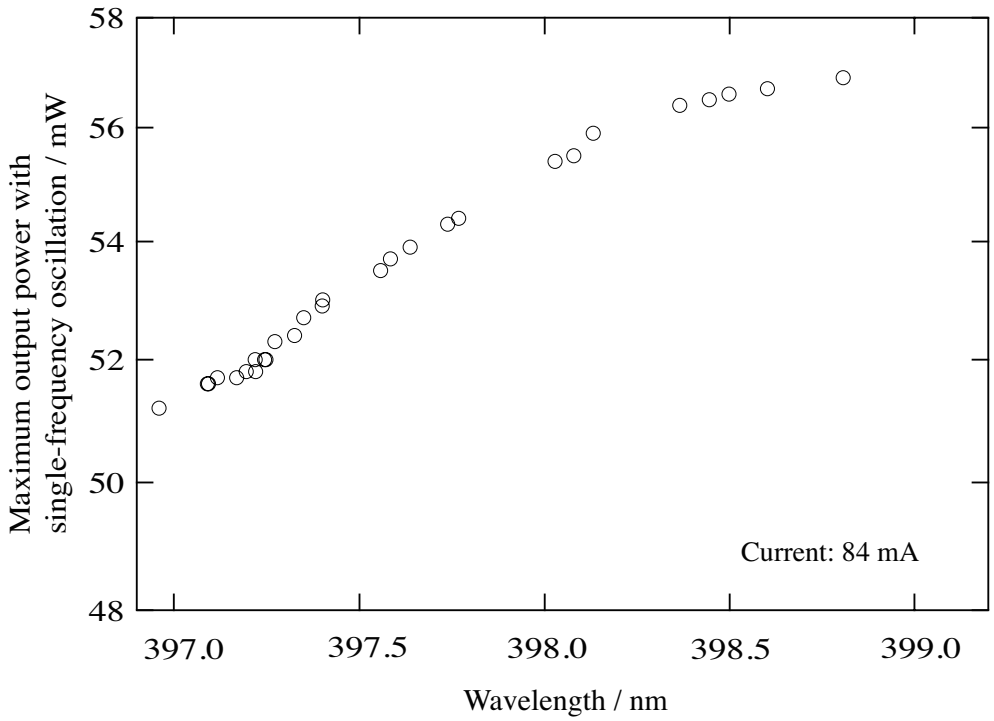

Fig. 3.8 Wavelength dependence of output power at maximum operation current with single-frequency oscillation. Wavelength tuning is achieved over 2 nm at the maximum operation current by rotating the diffraction grating.

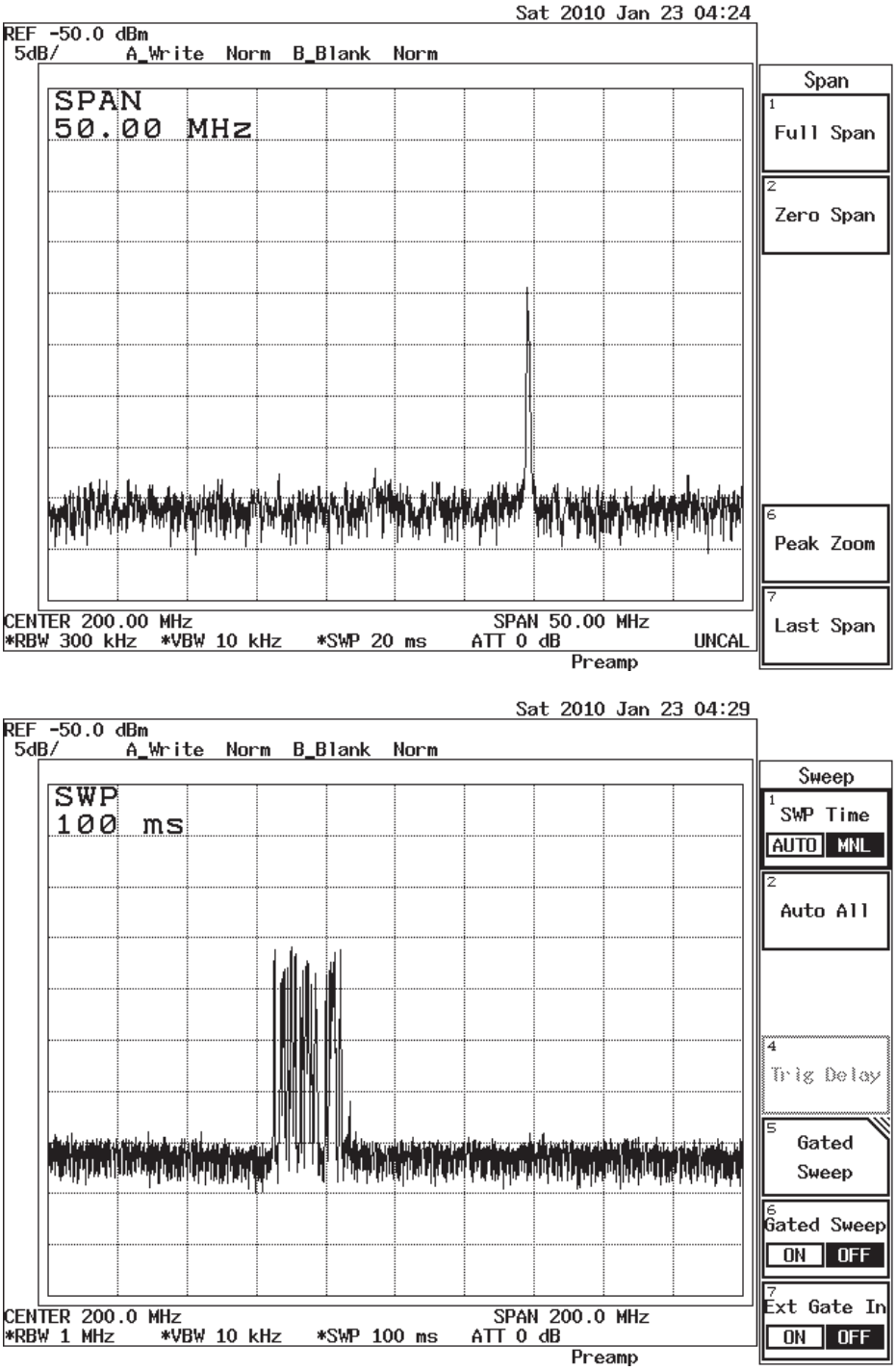

Fig. 3.9 Beat signals between ECLD and frequency-doubled Ti:S laser. Linewidth with single-frequency oscillation is obtained to be 2 MHz (upper figure) and 20 MHz (lower figure) for observation times of below 1 ms and 10 ms, respectively. The observation times are estimated from the sweep times of the RF synthesizer.

3.3 Saturated Absorption Spectroscopy of Yb Atoms in Hollow Cathode Lamp

As we described in the introduction part of this chapter, precise frequency tuning is required in the light source at 399 nm, with which we drive the $^1S_0 - {}^1P_1$ transition in Yb as the first-excitation for photoionization, in order to conduct isotope-selective loading. For this purpose, we detect saturated absorption (SA) signals of the transition. Saturated absorption is one of the techniques used in high-resolution spectroscopy and is applied to the detection of the transitions in atoms and molecules used to obtain reference frequencies. Even after employing SA, isotope shifts and hyperfine structures are sometimes incompletely resolved, and these unresolved lines contain signals of target isotopes required for subsequent investigations.

In this section, we describe a simple method to detect minor isotope lines in a SA spectrum by absorption filtering of major isotope lines. We investigate this method for the spectroscopy of the $^1S_0 - {}^1P_1$ transition by controlling the density of Yb atoms by varying the discharge current of a hollow cathode lamp (HCL). As we described in Sec. 1.1, $^{171}Yb^+$ is an attractive isotope in optical frequency standards because it is insensitive to the magnetic field. The natural abundance of the isotope 171 is small and 14%. Although, we develop this method for our future application to isotope-selective loading of Yb^+, it can be applied to other transitions of other atoms which are intended to selectively detect the lines of their minor isotopes.

3.3.1 Principle of selective detection of minor isotope lines

We describe the principle of the selective detection. We assume that the intensity of a pump beam is greater than the saturation intensity at the entrance of the sample of atoms. As we increase the density of atoms, a significant decrease in the pump beam intensity caused by linear absorption is observed, and finally, the pump beam intensity decreases below the saturation intensity before pump beam reaches the end of the sample. Under this condition, the probe beam, which enters the sample from the opposite side, is absorbed until it reaches the saturated part of the sample, i.e., we detect the SA signal

using a probe beam with a lower intensity. On the other hand, the number of atoms that contribute to the SA signal does not increase as we further increase the density of atoms. The number of atoms that contribute to the SA signal increases at the entrance of the sample. However, the depth at which the pump beam intensity decreases below the saturation intensity is inversely proportional to the density of atoms. Therefore, when the depth at which the SA signal is generated is smaller than the sample length, the SA signal grows smaller as we further increase the density of atoms because the number of atoms that contribute to the SA signal, which is detected using the weakened probe beam by linear absorption, remains approximately constant. As we increase the density of atoms, the above phenomenon is first observed in isotopes that have a high abundance and then in isotopes that have low abundance. Therefore, we can selectively detect the SA signal of minor isotopes by adjusting the appropriate density of the atoms.

We demonstrate this in a commercially available HCL by detecting the $^1S_0 - {}^1P_1$ transition. This transition is used for not only the loading of Yb^+ in an ion trap through photoionization but also the laser cooling of Yb [41]. The HCL is conveniently used to obtain the reference frequencies [42], and the density of the atoms is controlled by varying

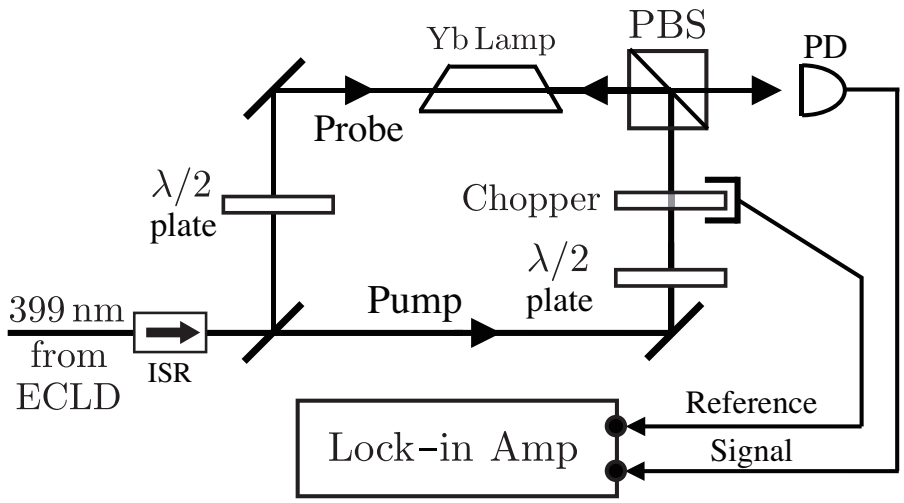

Fig. 3.10 Experimental setup of SA spectroscopy. PBS, polarizing beam splitter; PD, photodiode; ISR, isolator with isolation > 40 dB. The polarization of pump and probe lasers are tuned to be orthogonal each other by using the $\lambda/2$ plates.

the discharge current of the HCL.

3.3.2 Experimental setup and results

The experimental setup is shown in Fig. 3.10. The laser beam from the ECLD is split into a strong pump beam and a weak probe beam. The two beams are counterpropagated and overlapped in an HCL (Hamamatsu, L2783-70ANE-YB). The HCL contains a carrier gas comprising a mixture of Ar and Ne gases, which is injected into the HCL at pressures of 270 and 400 Pa. The powers of the pump and probe beams are 360 and 30 μW, respectively, at the window of the HCL. The scanning speed of the laser frequency is 15 MHz/s. To eliminate the component of linear absorption, the pump beam is chopped and the probe beam is detected at the chopping frequency by using a lock-in amplifier. The typical chopping frequency is 1170 Hz.

The SA spectra are shown in Fig. 3.11 as a function of the discharge current of the HCL. The lines of the isotopes and the hyperfine components are assigned by using the frequency intervals reported in the literature [43]. As described in Sec. 1.2, the natural abundance values of the Yb isotopes 176, 174, 173, 172, 171, 170, and 168 are 13, 32, 16, 22, 14, 3, and 0.1%, respectively. As the discharge current is increased, we first observe that all the lines grow larger in proportion to the increase in the density of Yb atoms. Above a discharge current of 2 mA, the signals of the major isotopes 172 and 174 grow smaller, whereas the signal of the minor isotope 171 becomes more distinct, as discussed above. Because the lines of the two major isotopes are located around the center of the entire absorption structure, the lines at the edge of the structure for the isotopes 176, 171, 170, and 168 remain even at a high discharge current of more than 5 mA. At a high current of more than 5 mA, the probe beam is absorbed by the lines of the isotopes 176, 171, and 170, and finally, we observe only the signal of the isotope 168, which is the rarest isotope. We can set the optimum discharge current for each isotope to detect the SA signal with the highest resolution. For example, for the isotope 171, which is used as an optical frequency standard [2, 44], the discharge current of 2.0–2.8 mA gives us the best resolution.

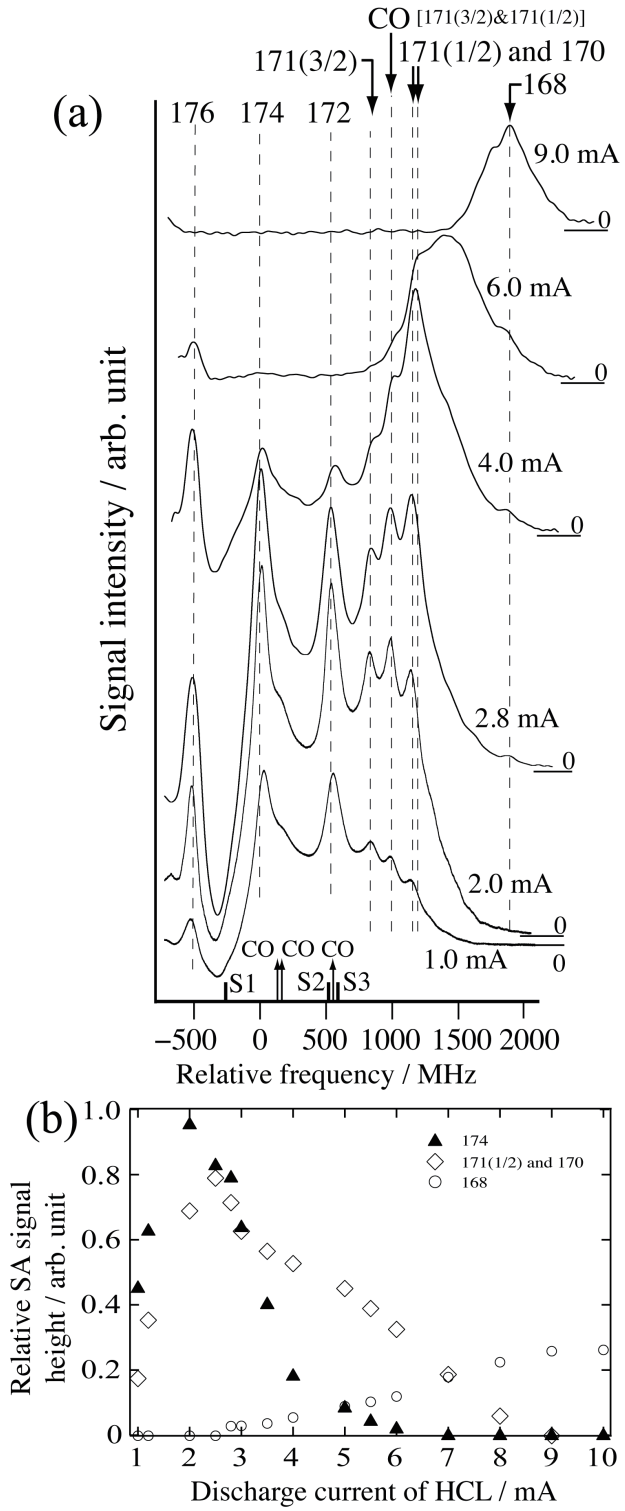

Fig. 3.11 Saturated absorption signals of $^1S_0 - {}^1P_1$ transition in Yb as a function of discharge current of HCL. (a) CO, crossover resonance. S1, S2, and S3 are transitions of 173(5/2), 173(3/2), and 173(7/2), respectively [43]. The number in parentheses represents the total angular momentum of the upper state of the transitions. (b) Dependence of SA signal height on discharge current for three isotope lines shown in the figure. We plot the peak height of the detected signals as the signal height for each line without the deconvolution of the components.

3.4 Summary

In this chapter, we describe the light sources for photoionization loading of Yb^+. We develop two tunable light sources at 399 nm and a precise frequency tuning method in order to realize a future application to isotope-selective loading of Yb^+ by using the $^1S_0 - {}^1P_1$ transition in Yb as the first-excitation of the two-color photoionization. Although we investigate them for our specified purpose, we obtain the results which can be more generally applied in various fields.

One of the light source at 399 nm is a frequency-doubled Ti:S laser. In order to increase the conversion efficiency to SH from radiation of a CW laser of which power is usually small, the nonlinear crystal which generates SH is placed in an external cavity. We demonstrate that the small residual surface reflection at the facets of a normal-cut nonlinear crystal markedly decreases the enhancement factor when the external cavity has high finesse. We propose that this problem is eliminated when the beams reflected at the two facets are subjected to constructive interference. We demonstrate a solution to the problem by temperature tuning of the BBO crystal used in our setup. A temperature change of at most 3 K is sufficient to achieve the maximum enhancement factor at any wavelength and this tuning range is much smaller than the phase-mismatching tolerance of the temperature.

The other is an ECLD, developed in order to simplify the light source at 399 nm. We use a high-power ultraviolet diode chip, which are very recently available. In order to realize single-frequency oscillation at the maximum output power, the cavity length shorter than 16 mm is effective.

In order to tune the lasers for driving the $^1S_0 - {}^1P_1$ transition as the first-excitation of photoionization, we detect SA signals. We demonstrate a simple method to detect the minor isotope lines in a SA spectrum by absorption filtering of major isotope lines. By using Yb atoms in a HCL, we separately detect the SA signals of the minor isotopes of 171 and 168, which is used in an optical frequency standard and is the rarest stable isotope, respectively.

Chapter 4

Photoionization loading of Ytterbium ions

In this chapter, we describe the main results of this study, i.e., the investigations of the loading rate of Yb^+ ions loaded through photoionization in a RF trap. First, we summarize preparations of the investigations: In Sec. 4.1, we describe the principle of the measurement of the relative and absolute (or number) loading rate. In Sec. 4.2, we summarize the experimental setup, except for that described in detail in the previous chapters. In Sec. 4.3, we describe the measurement procedure of the loading rate.

Then, the following sections are devoted to describe the results and analysis of the photoionization loading of Yb^+. In Sec. 4.4, we describe the investigations of the loading rate loaded through the two-color photoionization, where the $^1S_0 - ^1P_1$ transition in Yb is driven as the first-excitation and Yb atoms in the $^1P_1$ state are ionized by irradiation with another radiation as the second-excitation. We measure the dependence of the loading rate on the second-excitation wavelength, and determined the loading cross section which is useful for comparison to other systems. We detect the Rydberg states from the enhancement of the loading rate. In Sec. 4.5, we describe the measurement of the loading rate loaded through one-color photoionization conducted by irradiation only with the first-excitation laser. We discuss the ionization process of the one-color photoionization.

Finally, we describe the investigations of the charge exchange rate between Yb^+ and Yb. The charge exchange is one of the factors that limit the purity of the target isotope ion in isotope-selective photoionization loading. We measure the charge exchange rate

between from the shift of the secular frequency determined from the collective oscillation of different isotope ions, and discuss the effect of the charge exchange on the purity of the isotope-selectively loaded target isotope by using the loading rate and the charge exchange rate that we measured.

4.1 Principle of Measurement

As we described in Chap. 1, we drive the $^1S_0 - ^1P_1$ transition in Yb atoms at 398.912 nm as the first excitation of the photoionization. We simultaneously perform another irradiation to ionize Yb atoms in the $^1P_1$ state as the second excitation, except for the investigation of the one-color excitation. The energy diagram of Yb atoms related to the photoionization conducted in this work is shown in Fig. 1.2.

The density of trapped ions, n, during loading is given by the following equation [45]: $dn/dt = r - n/\tau - \zeta n^2$, where r is the density loading rate, i.e., the rate that ions are photoionized and trapped, τ is the lifetime in the trap determined from the loss rate due to the collisions with the residual background gases, and ζ is the loss rate due to ion-ion collisions. At the start of loading, the loss terms are negligibly small because $n \sim 0$ and the density loading rate can be determined from the increase in the density, i.e., $r = dn/dt|_{t=0}$. In electric resonance detection, we measure the number of trapped ions, N, instead of the density. We determine the number loading rate R as

$$R = dN/dt|_{t=0}\,. \tag{4.1}$$

In order to determine R, we conduct the following procedure. First, we measure the temporal gradient of the relative signal height $Y_{\max}$ of the electric resonance signal at the start of loading (we define this as the $Y_{\max}$ loading rate R_Y.). At the start of loading, the number of trapped ions is small and $Y_{\max}$ is close to 0. As we described in Sec. 2.2.1 $Y_{\max}$ is proportional to N where the number of trapped ions is small even in the presence of anharmonicity. Therefore, the uncertainty caused by anharmonicity and linearity deviation in the electric resonance detection is removed from R_Y. Therefore, we can compare the relative loading rate with various loading conditions by using R_Y. Then, after we measure the conversion factor $N/Y_{\max}$ as described in Sec. 2.2.1, we are able to determine R.

4.2 Experimental setup

We use the second-harmonics of radiation from the Ti:S laser, described in Sec. 3.1, as the radiation for the first excitation. ECLDs with four diode-laser chips of different oscillation wavelengths are used as second-excitation lasers. Diffraction gratings are arranged in the Littrow configuration. The beams of the first- and second-excitation lasers are overlapped and counterpropagated through the trap center. The two beams are focused with lenses of a focal length of 125 mm. Their beam waists are located at the center of the trap. The diameters of the beam waists of the first- and second-excitation lasers, measured outside the trap, are 90 μm and 60 μm, respectively. The frequency of the first-excitation laser is tuned as the fluorescence of the $^1S_0 - {}^1P_1$ transition of Yb atoms from the oven is maximized. The fluorescence is monitored with a CCD camera. Although the Ti:S laser is not actively frequency stabilized, the linewidth is below 1 MHz and the frequency drift is as slow as 1 MHz/s. The adjustment of the frequency during the ion production is only occasionally required when the production time is long. The wavelength of the second-excitation lasers are set using an optical spectrum analyzer (Advantest Inc., Q8347) having an uncertainty of 0.005 nm. This analyzer is also used to monitor the single-frequency oscillation of the second-excitation lasers. The RF trap used for the investigations of photoionization loading, and the parameters of the electric resonance detection have been described in Sec. 2.2.2.

4.2.1 Measurement procedure of loading rate

We measure the loading rate through the following procedure. (i) We switch the oven on and wait until it reaches a thermal equilibrium; this equilibrium is reached within five minutes and can be gauged by observing the fluorescence caused by the irradiation of the first-excitation laser. (ii) We switch the AC trapping voltage off in order to clear the trapped ions and then turn it on again. (iii) We immediately add the irradiation by the second-excitation laser. This is the time when the loading starts. (iv) After we continue loading for some time, we block the second-excitation laser and turn off the oven. The oven cools down rapidly, and the fluorescence at 399 nm disappears within 5 s. (v) We perform electric resonance detection by V_{dc}-sweep. The probe voltage is applied only at

this detection process. (vi) We repeat the procedure listed above, as we change the ion production time, i.e., the duration of irradiation by the second-excitation laser (process from (iii) to (v)). Between steps (ii) and (iii) and during step (iv), Yb atoms are irradiated with only the first-excitation laser for a few seconds. As discussed later, we found that the loading rate in case of irradiation only with the first-excitation laser is very slow and the modification of the loaded ion number is negligibly small.

Next, we plot the detected $Y_{\max}$ as a function of the ion production time. Samples are shown in Fig. 4.1(a). The $Y_{\max}$ loading rate R_Y is determined from the gradient at the start of the loading. We estimate the gradient by fitting the measured $Y_{\max}$ to the equation $Y_{\max} = A[1 - \exp(-R_Y\, t)]$, where A is a constant. The saturation in $Y_{\max}$ is caused not only by the balance of the rates of loading and loss but also by the characteristics of the electric resonance signal for a large number of ions [13, 21]. When the loading rate was slow, it was difficult to fit the result to the equation; hence, we instead used a polynomial equation for fitting.

4.3 Two-color photoionization

4.3.1 Dependance on second-excitation wavelength

We measure the dependence of the loading rate on the wavelength of the second-excitation laser. In order to ensure that the dependence is only on the wavelength of the second-excitation laser, the excitation of the first-transition of the $^1\mathrm{S}_0 - ^1\mathrm{P}_1$ is required to be saturated and the power of the second-excitation is adjusted to be in the range where the loading rate is proportional to the power. Therefore, we measured the power dependence of the loading rate, as shown in Fig. 4.1 (b), for a fixed wavelength of the second-excitation laser. The powers of the laser beams were measured at the window of the vacuum chamber. From the results, shown in Fig. 4.1 (b), we fixed the powers of the first- and second-excitation lasers to be 4 mW and 20 μW, respectively, when measuring the wavelength dependence.

The dependence of R_Y on the second-excitation laser wavelength is summarized in Fig. 4.1 (c). The most efficient wavelength in our measured wavelength range was close to that corresponding to the ionization potential. We quantitatively confirmed that the

cooling laser to drive the $^2S_{1/2} - {}^2P_{1/2}$ transition in Yb^+ at 370 nm was a suitable alternate to the second-excitation laser, as reported in [10]. The dependence of the loading rate on the second-excitation laser wavelength is similar to the dependence of the photoionization cross section from the $^1S_0$ ground state measured with a single photon from a synchrotron radiation [46]. The wavelength of 370 nm may be assigned in the low-energy wing of the $5d6p\,{}^3P_1$ autoionizing line [46]. The number loading rate R was obtained as $2.3(3) \times 10^3\,s^{-1}$ using the conversion factor N/Y_{max} as described in Sec. 2.2.3.

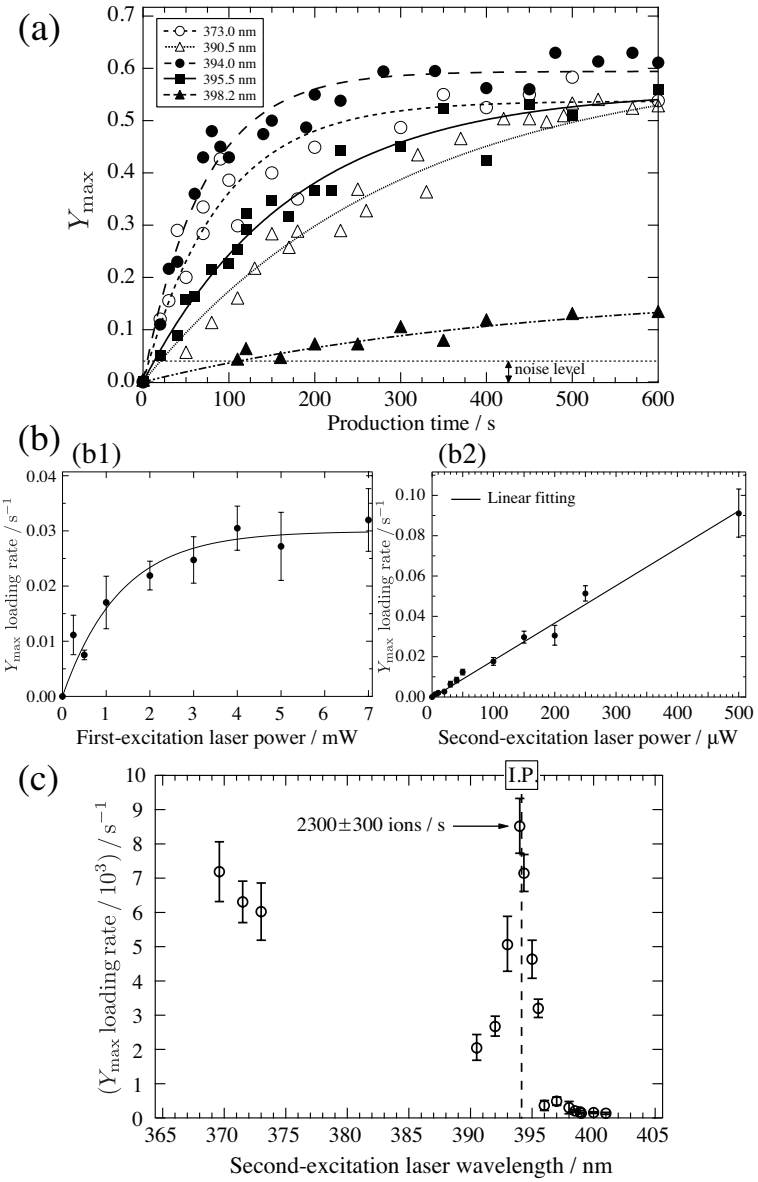

Fig. 4.1 Loading rate of $^{174}Yb^{+}$ by two-color photoionization as a function of the wavelength of second-excitation laser. The oven current is 3.0 A. (a) Increase in $Y_{\max}$ with the ion production time observed with several wavelengths of the second-excitation laser. Powers of the first- and second-excitation laser are 4 mW and 20 μW, respectively. (b) Loading rate of two-color photoionization as a function of (b1) the first-excitation-laser power and (b2) the second-excitation-laser power. In (b1), the second-excitation-laser power is 200 μW. In (b2), the first-excitation-laser power is 4 mW. The wavelength of the second-excitation laser is 392 nm. The $Y_{\max}$ loading rate shows a saturation to the first-excitation-laser power and a proportional increase with the second-excitation-laser power. From these results, we fix the powers of the first- and second-excitation laser to be 4 mW and 20 μW, respectively, when we measure the dependence on the wavelength of second-excitation laser. (c) Loading rate as a function of the wavelength of the second-excitation laser. The $Y_{\max}$ loading rate is determined from the gradient of $Y_{\max}$ at $t = 0$.

4.3.2 Determination of loading cross section

Using the number loading rate, we estimated the loading cross section σ_{L} from the equation [8]: $R = n_{\mathrm{a}} V \sigma_{\mathrm{L}} I/(h\nu)$, where $I/(h\nu)$ is the incident photon flux; I, the laser intensity; h, the Plank constant; and ν, the laser frequency; n_{a}, the density of the Yb atoms from the oven; and V, the volume of ionization. The density of the Yb atoms, n_{a}, can be measured from the absorption of the first-excitation-laser power at 399 nm by the Yb atoms.

We could not measure the absorption at the standard operational oven current of 3.0 A in this work, owing to low density. Therefore, we determined the density at the oven current of 3.7 A and measured the relative density using the fluorescence intensity, in order to estimate the density at the standard operational current. The loading rate at the oven current of 3.7 A was much faster than the response of our electric resonance detection system even when the power of the second-excitation laser was decreased. Therefore, the measurement of the relative density was required although this would be an additional source of uncertainty. The density n_{a} is estimated from the absorption spectrum by using the equation [47, 48]: $n_{\mathrm{a}} = (8\pi/\lambda^2)[g_1/(g_2 A_{21})] \int -(1/L)\ln[\, I(\nu)/I_0]\, \mathrm{d}\nu$, where λ is the wavelength of the transition, $g_i = 2J_i + 1$ ($i = 1, 2$: subscripts 1 and 2 indicate the lower and upper states, respectively.) is the weighting factor determined from the total angular momentum J_i, A_{21} is the Einstein coefficient of the transition, and $I(\nu)$ and I_0 are the transmitted and input laser intensities, respectively. By taking $A_{21} = 1.76 \times 10^8\,\mathrm{s}^{-1}$, $g_1 = 1$, and $g_2 = 3$, we obtained $n_{\mathrm{a}} = [2.7(5) \times 10^{12}\,\mathrm{m}^{-2}]L^{-1}$ at the oven current of 3.7 A.

The interaction length L is estimated from the divergence angle of the atomic beam θ using the relation: $L = 2l \tan[\theta/2]$, where l is the distance from the head of the oven to the trap center. The angle θ is derived from $\tan[\theta/2] = \bar{v}_\perp/\bar{v}_\parallel$, where $\bar{v}_\perp$ and $\bar{v}_\parallel$ are the transverse and longitudinal mean velocities, respectively, of the Yb atoms from the oven. We estimate $\bar{v}_\perp$ from the absorption spectra at the oven current of 3.7 A by fitting it with a Voigt profile. From the component of the Doppler width of 420(20) MHz, we estimated $\bar{v}_\perp$ to be 110(5) m/s.

The longitudinal mean velocity $\bar{v}_\parallel$ is estimated from the oven temperature. The oven temperature T_{oven} is indirectly estimated from the following equations: the ideal gas law

of $P = n_{\mathrm{oven}} k T_{\mathrm{oven}}$, where P is the atomic vapor pressure, n_{oven} is the atomic density in the oven, k is the Boltzmann constant; the Clausius-Clapeyron equation, which shows P as a function of T as described in Appendix B [49]; and the relation between n_{oven} and the density of the trap center, n_{a}, given by $n_{\mathrm{oven}} = n_{\mathrm{a}} \kappa L^2/d^2$, where d is the inner diameter of the oven and the factor $1/\kappa$ is given by $(1/\kappa) = (8/3)(d/2)/l_{\mathrm{oven}}$ for a cylinder oven, l_{oven} being the oven length [50]. From the known values of $l = 43(3)\,\mathrm{mm}$, $d = 0.65\,\mathrm{mm}$, and $l_{\mathrm{oven}} = 9\,\mathrm{mm}$, we obtain $T_{\mathrm{oven}} = 520(10)\,\mathrm{K}$, $\bar{v}_{\parallel} = 300(5)\,\mathrm{m/s}$, $\theta = 20(1)^\circ$, and $L = 17(1)\,\mathrm{mm}$. We observed the fluorescence through the mesh endcap electrode and roughly estimated $L = 19(3)\,\mathrm{mm}$, confirming the above estimation. Next, we determined $n_{\mathrm{a}} = 1.6(3) \times 10^{14}\,\mathrm{m}^{-3}$ at the oven current of 3.7 A. The relative density measurement was actually accomplished by measurement of the laser power required for generating the same fluorescence intensity. In this measurement, we adjusted the laser intensity well below the saturation intensity. The density ratio between the oven current of 3.0 A and 3.7 A was measured to be 260(60). To ensure that the comparison was performed well within the dynamic range of the relative fluorescence intensity measurement, we compared the intensity in small ranges of the oven current. In order to determine the density ratio between 3.7 A and 3.0 A, we compared the intensity between 3.7 A and 3.3 A, and then between 3.3 A and 3.0 A. The results of the relative density measurement are partly shown in Fig. 4.5 (b). The validity of the measurement is confirmed by the results that the charge exchange rate is in proportion to the determined relative fluorescence intensity, i.e., the relative density. Assuming that θ and L are unchanged beyond their uncertainties for the oven current value between 3.7 A and 3.0 A, we finally obtain $n_{\mathrm{a}} = 7(2) \times 10^{11}\,\mathrm{m}^{-3}$ at the oven current of 3.0 A. We estimate the loading cross section from the intermediate $^1\mathrm{P}_1$ state to the ionization potential at 394 nm to be 40(15) Mb ($1\,\mathrm{Mb} = 10^{-22}\,\mathrm{m}^2$). This value is comparable to that of Ca^+ [8] and larger than the photoionization cross section value of Yb^+, which was determined from enhancement of the decay rate constant of Yb atoms in a magnet-optical trap by irradiation of radiation at 370 nm [12].

4.3.3 Enhancement of loading rate by excitation to Rydberg state

We detected the excitation to the Rydberg states in Yb atoms from the increase in the loading rate. The results are shown in Fig. 4.2. Yb atoms were excited to the Ryd-

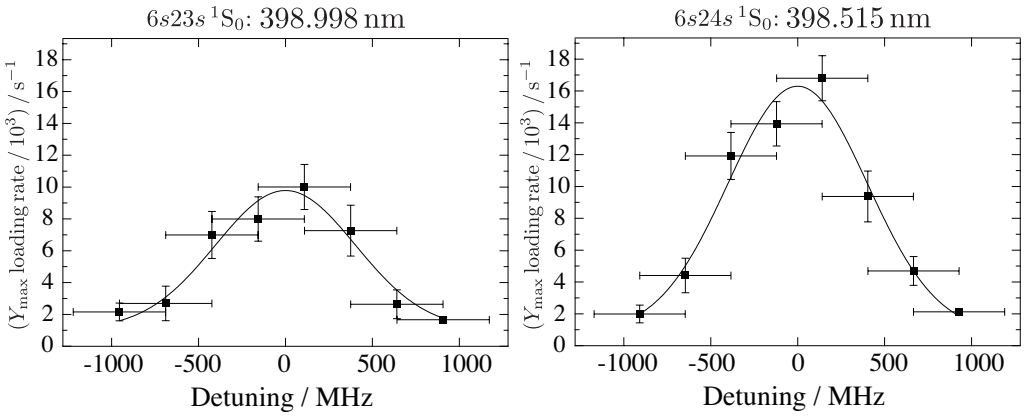

Fig. 4.2 Loading rate via Rydberg states. The center wavelengths of the second excitation to the $6s23s\,^1S_0$ and $6s24s\,^1S_0$ states are 398.998 nm and 398.515 nm, respectively. The second excitation laser, having a power of 5 mW, is frequency modulated by applying a triangle wave at 300 mHz to the PZT controlling the cavity length. The modulation width represented as the horizontal error bar is 500 MHz. The solid curve represents Gaussian profiles, and both full widths at half maximum are estimated to be 700 MHz.

berg states of $6s23s^1S_0$ and $6s24s^1S_0$ through second-excitation laser wavelengths around 398.998 nm and 398.515 nm, respectively [51]. In this excitation scheme, the intermediate and final states are the real states. Therefore, only the Yb atoms that were velocity-selectively excited to the $^1P_1$ intermediate state by irradiation with the first-excitation laser were excited to the Rydberg states with the second-excitation laser. The two lasers are required to have frequency stabilities of the order of the natural width of the $^1P_1$ state in order to efficiently excite the atoms to the Rydberg states. Instead of improving the frequency stabilities of the lasers, we frequency modulated the second-excitation laser to cover the frequency drifts. The frequency of the ECLD was modulated by applying a triangle-wave voltage at 300 mHz to the PZT controlling the cavity length. The modulation width is ± 250 MHz.

We measured the dependence of the loading rate on the second-excitation laser power, when we excited Yb atoms to the $6s23s\,^1S_0$ state as shown in Fig. 4.3. This dependence is found to be linear. This indicates that the possible ionization schemes from the $^1P_1$ state are resonant two-photon ionization using the Rydberg states as the second intermediate state or field-assisted ionization of Yb atoms in the Rydberg states.

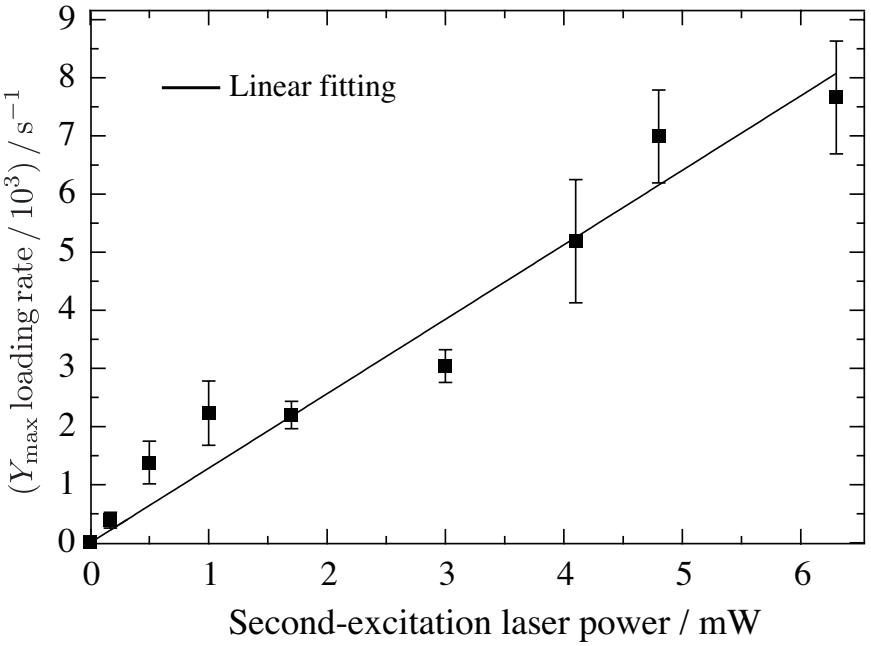

Fig. 4.3 Dependence of loading rate on power of second-excitation laser at 398.998 nm with which the Yb atoms are excited to the $6s23s\,^1S_0$ states. The frequency of the second-excitation laser is modulated with a triangle wave, in order to avoid decrease in the excitation rate caused by the frequency drift. The width and frequency of the modulation are 800 MHz and 300 mHz, respectively. The loading rate is closely proportional to the power of the second-excitation laser.

4.4 One-color Photoionization

The photoionization loading of Yb^+ was first conducted for irradiation by only the first-excitaion laser at 399 nm [11], although the total energy of the two photons at 399 nm is below the ionization potential. This one-color photoionization process is explained as the combination of the following effects [3, 10]: (i) lowering of the ionization threshold by the trapping electric field [47] and (ii) off-resonant excitation of Yb atoms in the $^1P_1$ state to the Rydberg states and their subsequent field ionization or direct photoionization by absorption of only one more photon from the $^1P_1$ state.

Figure 4.4 shows the dependence of the loading rate on the power of the first-excitation laser. If the proposed processes are valid, the loading rate should be in proportion to the laser power. The experimental results showed that the power dependence was rather

quadratic. Therefore, we conclude that the non-resonant two-photon absorption from the $^1P_1$ state is the dominant process in the one-color photoionization. The excitation rate of non-resonant two-photon absorption is inversely proportional to the detuning between the virtual intermediate state and the real states around the virtual state. Several Rydberg states act as these real states with the increase in the excitation rate [52].

We also found that the loading rate is in proportion to the density of Yb atoms from the oven. Therefore, ionization of Yb atoms in the Rydberg states by collision with Yb atoms from the oven, another possible ionization process, is not observed.

We compare the loading rate of one-color excitation to that of two-color excitation. We adjust the one-color loading rate so that for the same Yb atomic density, the oven current is 3.0 A and the first-excitation laser power is 4 mW; as these values were used for the investigations of two-color photoionization. Then, we found that the loading rate

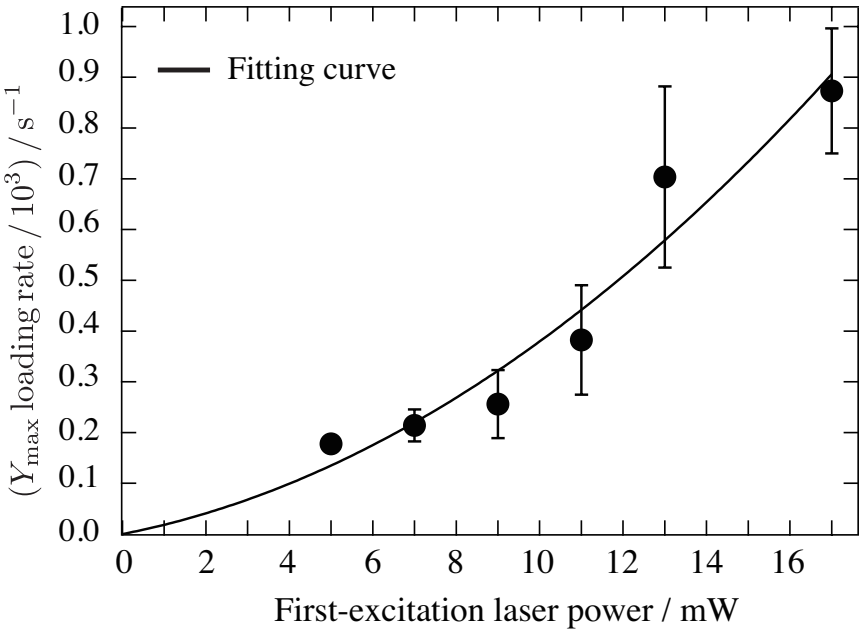

Fig. 4.4 Dependence of loading rate on power of first-excitation laser when Yb atoms are irradiated with only the first-excitation laser tuned to the $^1S_0 - {}^1P_1$ transition at 398.912 nm. The oven current was set to 3.3 A, because the ions are not detected when the oven current is at 3.0 A, the value at which the other measurements were conducted. When the laser power was below 5 mW, no ions were detected. The results are fitted by a quadratic function. The component quadratically increasing with the first-excitation laser power was clearly observed.

of one-color excitation was 1000 times smaller than that of two-color excitation at the second-excitation wavelength in the vicinity of the ionization potential or of the cooling transition of Yb^+. On the other hand, Balzer *et al.* reported that the loading rate of one-color excitation was only 10 times smaller than that of two-color excitation [10]. It is impossible to discuss this discrepancy because the intensity of the cooling laser for Yb^+ is not provided in [10]. However, one possible reason for the discrepancy might be a difference in the trapping electric field strength due to the difference in the trap size. The electric field ionization thresholds of the Yb Rydberg states are reported to be a few kV/cm, e.g., 2.72 kV/cm for the $6s23s\,^1S_0$ Rydberg state [53]. The effective electric field of our trap is 70 V/cm and below the threshold. On the other hand, the electric field of an ordinary miniature ion trap like the one used in [10] is comparable to the threshold.

4.5 Measurement of Charge Exchange Rate

When one conducts isotope-selective photoionization loading from an isotope mixture of an atomic source using the isotope shifts in the intermediate state, the charge exchange among the other isotopes of the atoms is one of the factors that limit the purity of the target isotope ion [8]. We measured the charge exchange rate between Yb^+ ions and Yb atoms through electric resonance detection and studied the effect of the charge exchange on the isotope-selective loading. The measurement of the charge exchange rate is conducted by detection of a collective oscillation of two isotopes of Yb^+ with the electric resonance. The collective oscillation is described in Sec. 2.3. We prepare a single isotope of trapped Yb ions, collide them with the other isotope of Yb atoms, and then measure the resonance frequency or $V_{\rm dc}$ as a function of time. We can determine the charge exchange rate from the temporal variation of the resonance $V_{\rm dc}$.

The experimental procedure is as follows. First, we turn on two ovens: one contains enriched 171 isotope and the other, 174. Then, only ^{171}Yb is isotope-selective photoionized by using the isotope shift in the $^1S_0 - {}^1P_1$ transition. Next, when the number of trapped ^{171}Yb ions reaches $Y_{\rm max} = 0.3$, we stop loading by turning off only the 171 oven and blocking the beams of the photoionization lasers. This is the time when the charge exchange starts. We finally perform the electric resonance detection by $V_{\rm dc}$-sweep after we wait some time in the process of the charge exchange. We repeat this measurement

by changing the waiting time. The laser is tuned by monitoring the fluorescence of ^{171}Yb atoms. In order to avoid the charge exchange during the loading, we increased the second-excitation-laser power and reduced the loading duration to less than 10 s. The isotope selectivity in this measurement is sufficient because no difference is observed between the resonance $V_{\rm dc}$ in this measurement and the resonance $V_{\rm dc}$ obtained when only one of the two ovens was operated. The relative signal height, i.e., the total number of trapped ions, is unchanged, and loss is not observed during the charge exchange process. This also indicated that the loss by RF heating caused by elastic collision with Yb atoms is negligibly small [54, 55]. This is because the density of Yb atoms at the oven current of 3.0 A was over four orders of magnitude smaller than that of the helium buffer gas.

Figure 4.5 shows the results of the charge exchange experiments. We fitted the results shown in Fig. 4.5 (a) by an exponential curve, and the charge exchange rate was obtained at the start of the exchange as for the measurement of the loading rate. The change in resonance $V_{\rm dc}$ can be approximated to be proportional to the change in the secular frequency in this small range. From the change in the frequency of the collective secular motion, we can determine the ratio of the number of the two isotopes as described above. The ratio is approximately proportional to the secular frequency because the relative mass difference ($= 3/172.5$) is small. Figure 4.5 (b) shows the charge exchange rate as a function of the relative density of the Yb atoms from the oven. The relative density was determined as described in Sec. 4.3. We conducted one measurement by interchanging of the isotopes of the ions and the atoms to be exchanged. As simultaneously shown in Fig. 4.5, we confirmed that the initial and the final resonance $V_{\rm dc}$ were completely interchanged and we measured a similar charge exchange rate. We determine the charge exchange cross section $\sigma_{\rm E}$ from the equation of the charge exchange rate $\gamma = \sigma_{\rm E} n_{\rm a2} \bar{v}$, where $n_{\rm a2}$ is the density of the atoms from the oven and $\bar{v}$ is the relative velocity between the trapped Yb^+ ions and Yb atoms from the oven. If the energies of the trapped Yb^+ ions and Yb atoms from the oven have Gaussian distribution, the relative velocity is given by the root mean square of each mean velocity [56]. The temperature of Yb atoms is estimated in Sec. 4.3. The temperature of the trapped Yb^+ ions is supposed to be 1200(700) K from the measurements using a similar trap and helium buffer-gas pressure [25]. We estimate the mean relative velocity to be 490(80) m/s, from which we obtain $\sigma_{\rm E} = 4(2)\times10^5$ Mb at the oven current of 3.0 A. This value is 10 times the theoretical value [18]. One possible reason for this

discrepancy is the spacial distribution of the atomic density of the Yb atoms from the oven. The ions are confined in a smaller region than the atomic flux, and we measured the average atomic density in the laser beam by the absorption method. Therefore, the atomic density at which the ions were trapped would be higher than the average density, and the value of σ_{E} measured by us should be an upper limit.

4.5.1 Effect on isotope-selective photoionization loading

We discuss the effect of the charge exchange on the isotope selective loading. A simple rate analysis of the isotope-selective loading including the charge exchange process is discussed as follows. When we load a specific isotope through photoionization of an isotope mixture of an atomic source, the numbers of trapped specific isotope ions, $N_i\,(i=1,2)$, can be expressed as

$$\begin{aligned} \frac{dN_1}{dt} &= R - \frac{1}{\tau}N_1 - \gamma_{21}N_1 + \gamma_{12}N_2 \\ \frac{dN_2}{dt} &= \quad -\frac{1}{\tau}N_2 + \gamma_{21}N_1 - \gamma_{12}N_2 \end{aligned}, \tag{4.2}$$

where the subscripts 1 and 2 indicate a target isotope and an unwanted isotope, respectively. R is the loading rate of a target isotope ion, τ is the lifetime of the trapped ions, and γ_{ij} is the charge exchange rate for a single ion. This rate is expressed as $\gamma_{ij} = \sigma_{\mathrm{E}} n_{\mathrm{a}j}\bar{v}\,(i=1,2)$, where σ_{E} is the charge exchange cross section, $n_{\mathrm{a}j}$ is the density of an isotope of atoms to be exchanged, and $\bar{v}$ is the relative mean velocity between the trapped ions and the atoms. We assume that there are no differences in $\sigma_{\mathrm{E}}, \bar{v}$, and τ between the isotopes. The photoionization of unwanted isotope atoms, which should be observed in a practical setup, is neglected in order to discuss only the effect of the charge

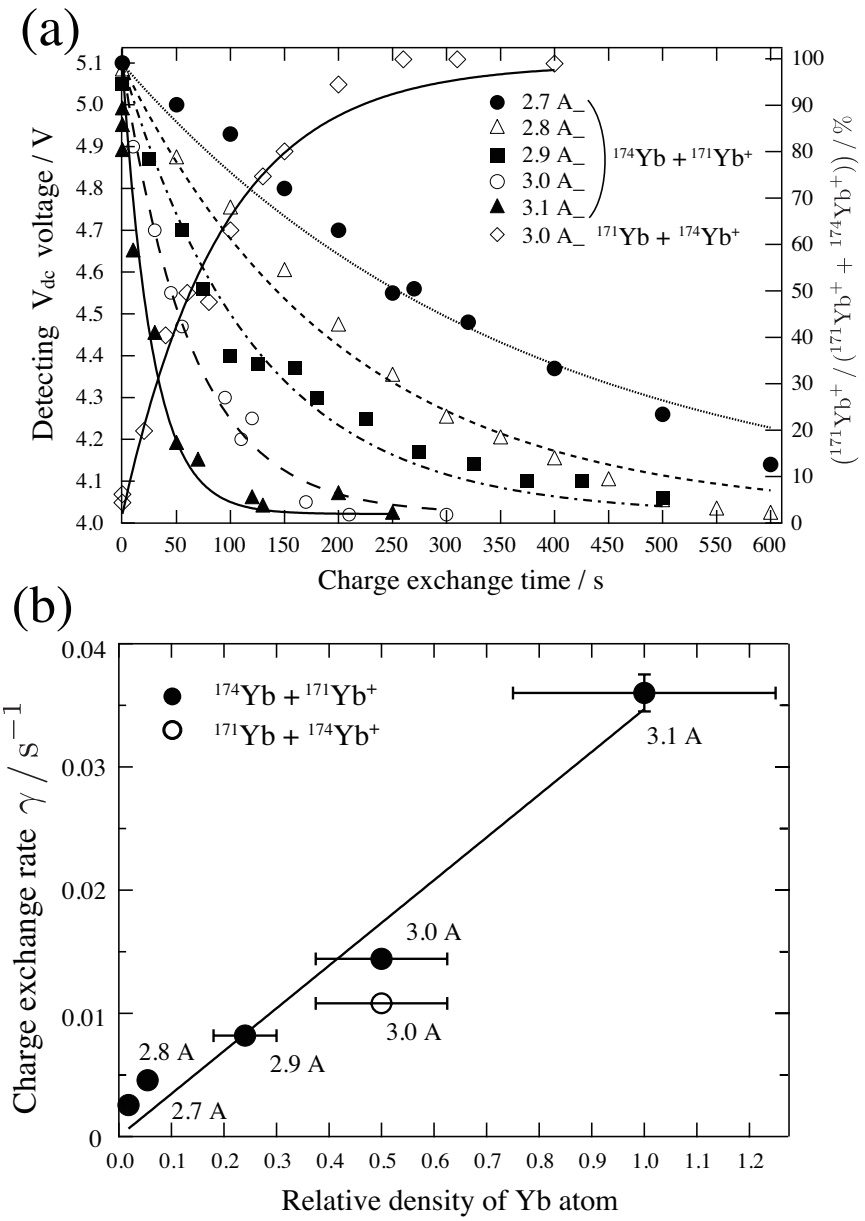

Fig. 4.5 Charge exchange rate between Yb^+ ions and Yb atoms. We use enriched 171 and 174 isotope as atomic sources. We prepare the trapped $^{171}Yb^+$ ions and collide them with ^{174}Yb atoms from the oven, except for one sample that the isotopes of the ions and the atoms to be exchanged are interchanged. (a) Temporal change of resonance V_{dc} by charge exchange collision of the exchange isotope for various values of oven current. The experimental procedure is shown in the text. The resonance V_{dc} for the pure $^{171}Yb^+$ ions and $^{174}Yb^+$ ions are 5.1 V and 4.0 V, respectively. The right axis shows the relative number of $^{171}Yb^+$ corresponding to the resonance V_{dc}. This is directly calculated from the related equations but is approximated to be proportional to resonance V_{dc}, as explained in the text. (b) Charge exchange rate as a function of the relative atomic density. The corresponding oven current is indicated in the figure. The relative atomic density was determined, as discussed in Sec. 4.3. The solid line represents the linear fitting to the data indicated by the black circles.

exchange. In the conditions above, subscript 2 can be regarded as a sum of unwanted isotopes.

When the lifetime of the trapped ions is negligibly small, i.e., $\tau^{-1} \ll \gamma_{ij}$ and $\tau^{-1} \ll R$, the second equation of Eq. (4.2) shows that the ratio of the target isotope ions decreases in time and it becomes equal to the abundance of the target isotope of the atomic source. This is independent of the loading rate R. (The loading rate just determines the total number of the trapped ions N_0 by the relation $N_0 = R\tau$.) If we intend to retain a high concentration of the target isotope ion, we need to stop loading before the process reaches the equilibrium. We can provide a measure of the best loading duration as $0.1\gamma_{21}^{-1}$, when we intend to trap as many target isotope ions as possible while we retain the concentration $N_1/(N_1 + N_2)$ to be approximately 0.9. We numerically determine the time when the concentration $N_1/(N_1 + N_2)$ decreases to 0.9 by solving Eq. (4.2) in the case of the standard condition of this work, i.e., the second-excitation laser wavelength and power are 394.1 nm and 20 μW, respectively. We found that $0.1\gamma_{21}^{-1}$ is approximately half of the values obtained from the numerical calculation. Thus, this measure is useful. In the standard operational condition of this work, $0.1\,\gamma_{21}^{-1}$ is estimated to be 8 s and 7 s for $^{171}\mathrm{Yb}^+$ and $^{168}\mathrm{Yb}^+$, respectively. $^{171}\mathrm{Yb}^+$ with a natural abundance of 14% is a useful isotope in the frequency standard, and $^{168}\mathrm{Yb}^+$ of 0.1% is the rarest stable isotope.

We can also introduce a measure of the maximum number of target isotope ions that are purely isotope-selective loaded. At the start of the loading, the first equation in Eq. (4.2) can be approximated as

$$\frac{dN_1}{dt} = R - \gamma_{21} N_1 \,, \tag{4.3}$$

because $N_2 \sim 0$. We can use the steady-state number N_{10} determined from Eq. (4.3) as a measure of the maximum number of target isotope ions that are purely isotope-selective loaded:

$$N_{10} = \frac{R}{\gamma_{21}} = \frac{(I/h\nu)V}{\bar{v}} \frac{\sigma_{\mathrm{L}}}{\sigma_{\mathrm{E}}} \frac{\eta}{1-\eta} \,, \tag{4.4}$$

where $\eta = n_{\mathrm{a1}}/(n_{\mathrm{a1}} + n_{\mathrm{a2}})$ is an abundance of the target isotope in an atomic source. The density of the neutral atoms has no influence on the purely isotope-selective loaded number; it only changes the best loading duration. We numerically determine the number of the loaded target isotope ions at the time when the concentration of the target isotope decreases to 0.9 by directly solving Eq. (4.2). The results are shown in Fig. 4.6 as an

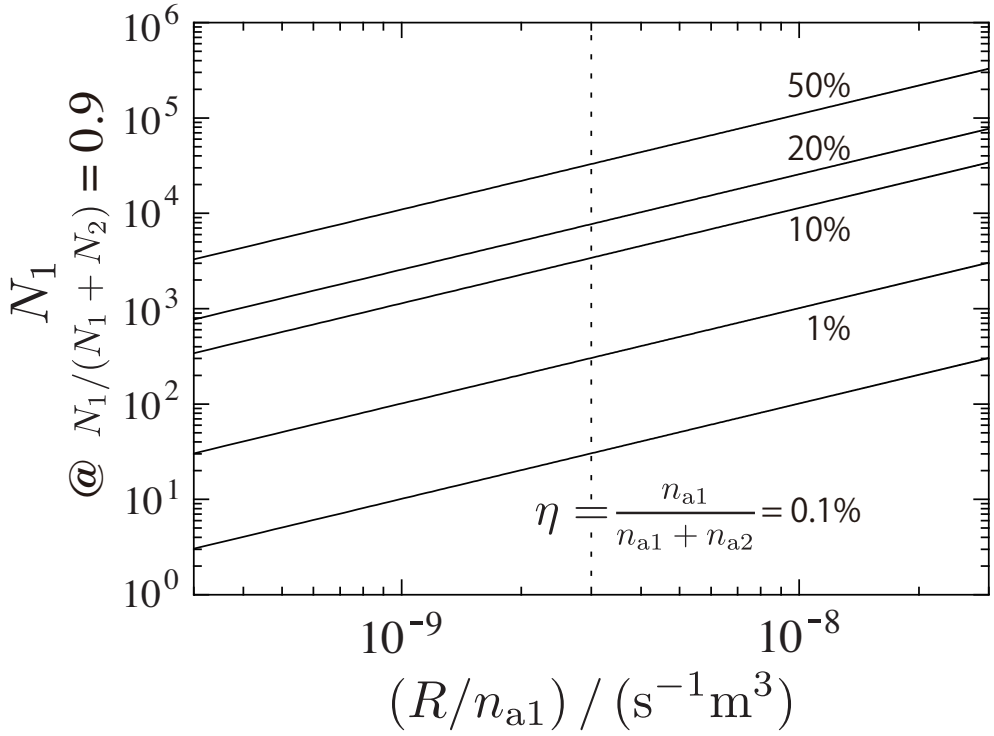

Fig. 4.6 The number of target isotope ions, N_1, at the time when concentration of $N_1/(N_1+N_2)$ decreases to 0.9; this number is obtained by directly solving Eq. (4.2). The results are shown as a function of $R/n_{a1} = \sigma_L VI/(h\nu)$, i.e., the loading rate per the atomic density. The abundance of the target isotope η is a parameter. The calculation is performed under our experimental conditions: the ionization volume is 0.3 mm^3, the density of the atoms is 7×10^{11} m^{-3} at the oven current of 3.0 A, and the lifetime of the trapped ions is 10^4 s. The standard condition of this work, i.e., the wavelength and the power of second excitation laser of 394.1 nm and 20 μW, respectively, corresponding to $R/n_{a1} = 3\times10^{-9}$ s^{-1}m^3, is shown by the dashed line.

abundance of the target isotope in the atomic source is a parameter. N_{10} is five times N_1 at the time when the concentration decreases to 0.9 . This demonstrates that N_{10} is a good measure of the maximum number of ions that are purely isotope-selective loaded.

If we consider the standard condition of this work, i.e., the wavelength and the power of second-excitation laser of 394.1 nm and 20 μW, respectively, we expect $N_{10} \sim (2\times10^5)\,\eta/(1-\eta)$, where η is the abundance of the target isotope in the atomic source. If we use a natural isotope mixture as a source, we expect that 3×10^4 and 200 ions are purely selectively loaded for $^{171}Yb^+$ and $^{168}Yb^+$, respectively. The loading rate proportionally

increased as the second-excitation-laser power is increased at least up to 500 μW in our measurement. This improves N_{10} by a factor of at least 25 as compared to the values estimated above. We can conclude that the charge exchange is not a significant factor for limiting the ratio of the number of the target isotope ions purely isotope-selective loaded with photoionization, as long as the abundance of the target isotope is not very low. In the ordinary setup, however, the atomic flux from the oven is not well collimated and the residual Doppler broadening degrades the selective excitation of the target isotope.

4.6 Summary

We have quantitatively investigated the loading rate of Yb^+ ions loaded through photoionization into an RF trap using the electric resonance detection. In the two-color photoionization, where the $^1S_0 - ^1P_1$ transition in Yb atoms is driven as the first excitation, we measure the dependence of loading rate on the wavelength of the second-excitation laser. The loading rate has a peak at 394.1 nm, which corresponds to the ionization potential from the $^1P_1$ state. The loading rate at 369.5 nm, which is the cooling wavelength of Yb^+, is similar to that at 394.1 nm. As Balzer *et. al* reported, we quantitatively confirmed that the cooling laser for Yb^+ is a substitute for the second-excitation laser in the two-color photoionization. The Rydberg states in Yb atom are detected by the enhancement of the loading rate. In one-color photoionization, we conclude that the non-resonant two-photon absorption from the $^1P_1$ state is the dominant ionization process.

As we apply the number estimation method, which we improved to be useful in the presence of anharmonicity, described in Sec. 2.2.1, we estimate the loading cross section to be 40(15) Mb at the second-excitation wavelength of 394.1 nm. The uncertainty in the loading cross section is limited by those in the estimation of other parameters such as density.

We have also investigated the charge exchange between trapped Yb^+ ions and Yb atoms from the oven, which is ones of the factors that limits the purity of the target isotope ion in isotope-selective photoionization loading. The charge exchange rate is measured from the shift of the collective oscillation of the secular motion. By analyzing the purity of the target isotope ion from the photoionization loading rate and the charge exchange rate that

we measured, we found that the charge exchange is a significant, only when the abundance of the target isotope is smaller than 0.1% in our photoionization scheme of Yb. On the other hand, the loading duration is required to be much smaller than the inverse of the charge exchange rate, otherwise the purity of the target isotope ions degrades and become equal to the abundance of the atomic source.

Chapter 5

Summaries

5.1 Summary of this study

In this thesis, we investigate the loading rate of Yb^+ produced by photoionization into a RF trap. The summary of each chapter is as follows.

In Chap. 1, we describe the background and the purpose of this study. Yb^+ is a suitable ion species for use in optical frequency standards and as a qubit in quantum information processing. Recently, photoionization has been widely used for loading of ions into a trap, because of several advantages such as high efficiency and isotope selectivity. Although photoionization loading of Yb^+ has been applied in several studies, it has not been quantitatively investigated so far. We investigate it by using an electric resonance detection of the ions trapped with buffer-gas cooling. In this method, we can remove the cooling efficiency from the loading rate because of high efficiency of buffer gas cooling unlike the measurement by using the ions trapped with laser cooling. One can determine the number of trapped ions from the electric resonance signal, which enable us to estimate the loading cross section. The loading cross section is useful for comparison with other systems.

In Chap. 2, we describe a method for estimating the number of trapped ions in a RF trap, using the electric resonance detection of the secular motion of trapped ions. The number of trapped ions are proportional to the product of the signal height and width of the electric resonance signal. However, the signal is distorted by an anharmonicity in the secular motion originated from a deviation from the harmonic potential. This is always observed in the traps ordinarily designed. The anharmonicity causes a hysteresis

in the signal which increases the signal width, and hence, an uncertainty in the number estimation is increased. We improve the number estimation method even in the presence of anharmonicity by fitting the signal with an equation derived from the Duffing equation. We evaluate the ion number with an uncertainty of 10%.

In Chap. 3, we describe the development of light sources for photoionization of Yb. We obtain three results that can be widely applied to other systems. They are related with the light sources at 399 nm with which the $^1S_0$–$^1P_1$ transition in Yb atoms is driven. The light source is required to be a single-frequency oscillation and continuous-frequency tunable in order to apply it to isotope-selective photoionization loading. During most of this study, it was difficult to realize a light source with such performance at 399 nm by direct laser oscillation. Therefore, we first generate the radiation at 399 nm by SHG using an external cavity technique, which is applied in order to improve the conversion efficiency. When an antireflection-coated normal-cut nonlinear crystal is used in an external cavity, a small residual reflection at the crystal facets causes a round-trip loss and prevents the realization of a large fundamental enhancement even when the external cavity has a high finesse. We propose that this problem is eliminated when the beams reflected at the two facets are subjected to constructive interference. We demonstrate a solution by a temperature tuning of the BBO crystal used as a nonlinear crystal in our setup. A temperature change of at most 3 K is sufficient to achieve the maximum enhancement factor by the constructive interference at any wavelength. We achieve an enhancement factor of 125, and a second-harmonic power of 125 mW is generated at 399 nm from a fundamental power of 390 mW.

Second, we realize single-frequency oscillation in an ECLD using a high-power ultraviolet diode chip. At the cavity length shorter than 16 mm, we obtain single frequency oscillation at the maximum output power of the chip. We measure the tuning range and the linewidth to be 2 nm and below 2 MHz for the observation time of 1 ms, respectively.

Third, we develop a simple method to detect the minor isotope lines in a saturated absorption spectrum by absorption filtering of major isotope lines. This is demonstrated for the saturated absorption spectroscopy of the $^1S_0 - {}^1P_1$ transition in Yb at 399 nm by controlling the density of Yb atoms by varying the discharge current of a hollow cathode lamp. Each isotope line has its optimum discharge current to achieve the highest resolution. We can enhance the lines of the most useful isotope of 171 as well as that of the

rarest isotope of 168.

In Chap. 4, we investigate the loading rate of Yb^+ ions loaded through photoionization into a RF trap. In two-color photoionization, where the $^1S_0 - {}^1P_1$ transition in Yb is driven as the first excitation and the second excitation laser ionizes the Yb atoms in the $^1P_1$ state, we measure the dependence of the loading rate on the second-excitation wavelength. The loading rate has a peak at the second-excitation wavelength of 394.1 nm, which corresponds to excitation to the ionization potential. A similar loading rate is observed at the second-excitation wavelength around 369.5 nm, which is the wavelength of the cooling transition of Yb^+. Thus we quantitatively confirmed that the cooling laser for Yb^+ is a good substitute for the second-excitation laser. We can detect the Rydberg states by the enhancement of the loading rate. In one-color photoionization, where the ionization is conducted by irradiation with only radiation at 399 nm, the non-resonant two-photon absorption from the $^1P_1$ state is the dominant ionization process. The loading rate of the one-color photoionization is measured to be three orders magnitude smaller than that of the two-color photoionization at the second-excitation wavelength of 369.5 nm or 394.1 nm. The ratio of the loading rate between the two-color and one-color photoionization is two orders magnitude smaller than that reported by Balzer *et al.*. One possible explanation of the discrepancy is the difference in the rate of the field ionization caused by the electric field of the trap, owing to the difference in the trap size. By using the improved number estimation method described in Chap. 2, we estimate the loading cross section to be 40(15) Mb at the second-excitation wavelength of 394.1 nm. The uncertainty is limited mainly by estimation of the density of Yb atoms.

We also measure the charge-exchange rate between Yb^+ and Yb atoms from the oven, which is one of the factors that limit the purity of the target isotope ion in isotope-selective photoionization loading. We estimate the charge exchange cross section to be $4(2)\times10^5$ Mb. From the photoionization and charge-exchange rates, we analyze the effect of the charge exchange on the isotope-selective photoionization loading. The charge exchange is a significant factor in limiting the number of target isotope ions that are purely isotope-selectively loaded, only when the abundance of the target isotope is smaller than 0.1% in our photoionization scheme of Yb, i.e., the rarest isotope of 168 is loaded. On the other hand, the loading duration is required to be much smaller than the inverse of the charge-exchange rate, otherwise the purity of the target isotope ion degrades and

converges to the abundance of the atomic source.

5.2 Future prospect

In this study, we use a large ion trap which has a trap region larger than the ionization region, and we trap the ions with buffer-gas cooling which is high efficient. Therefore, we suppose that the capture efficiency of the ionized atoms in the trap should be close to the unity and the loading cross section estimated in our work is approximately the same as the ionization cross section. The uncertainty in the loading cross section is limited mainly by that in the measurement of the atomic density. This could be improved. Therefore, our measurement method of the loading rate has a potential to be a method for measurement of the ionization cross section.

Some techniques developed for accomplishment of this study are useful for other studies. The number estimation method using the electric resonance signal is improved to be applicable even in the presence of anharmonicity which always accompanies the usual trap design. The method of eliminating the loss by the residual reflection at the anti-reflection-coated facets of the normal-cut nonlinear crystal in an external cavity for SHG can be applied to other materials used as nonlinear crystals. A high output power ultraviolet ECLD can be applied to laser cooling of Yb atoms. A method for selective detection of minor isotope lines in a saturated absorption spectrum is useful for various transitions of other atoms and ions.

Bibliography

[1] C. W. Chou, D. B. Hume, J. C. J. Koelemeij, D. J. Wineland, and T. Rosenband, "Frequency comparison of two high-accuracy Al^+ optical clocks", Phys. Rev. Lett. **104**, 070802 (2010).

[2] T. Schneider, E. Peik, and C. Tamm, "Sub-hertz optical frequency comparisons between two trapped $^{171}Yb^+$ ions", Phys. Rev. Lett. **94**, 230801 (2005).

[3] K. Hosaka and S.A. Webster and A. Stannard and B.R. Walton and H.S. Margolis and P. Gill, "Frequency measurement of the $^2S_{1/2} - ^2F_{7/2}$ electric octupole transition in a single $^{171}Yb^+$ ion", Phys. Rev. A **79**, 033403 (2009).

[4] S. Olmschenk and K.C. Younge and D.L. Moehring and D.N. Matsukevich and P. Maunz and C. Monroe, "Measurement of the lifetime of the $6p\,^2P^o_{1/2}$ level of Yb^+", Phys. Rev. A **80**, 022502 (2009).

[5] Y. Takasu and Y. Takahashi, "Quantum degenerate gases of ytterbium atoms", J. Phys. Soc. Jpn. **78**, 012011 (2009).

[6] N. Kjærgaard and L. Hornekær and A.M. Thommesen and Z. Videsen and M. Drewsen, "Isotope selective loading of an ion trap using resonance-enhanced two-photon ionization", Opt. Lett. **71**, 207 (2000).

[7] S. Gulde, D. Rotter, P. Barton, F. Schmidt-Kaler, R. Blatt, and W. Hogervorst, "Simple and efficient photo-ionization loading of ions for precision ion-trapping experiments", Opt. Lett. **73**, 861 (2001).

[8] D.M. Lucas and A. Ramos and J.P. Home and M.J. McDonnell and S. Nakayama and J.P. Stacey and S.C. Webster and D.N. Stacey and A.M. Steane, "Isotope-selective photoionization for calcium ion trapping", Phys. Rev. A **69**, 012711 (2004).

[9] U. Tanaka, H. Matsunishi, I. Morita, and S. Urabe, "Isotope-selective trapping of rare calcium ions using high-power incoherent light sources for the second step of photo-ionization", Appl. Phys. B **81**, 795 (2005).

[10] C. Balzer, A. Braun, T. Hannemann, C. Paape, M. Ettler, W. Neuhauser, and C. Wunderlich, "Electrodynamically trapped Yb^+ ions for quantum information processing", Phys. Rev. A **73**, 041407 (2006).

[11] K. Hosaka and S.A. Webster and P.J. Blythe and A. Stannard and D. Beaton and H.S. Margolis and S.N. Lea and P. Gill, "An optical frequency standard based on the electric", IEEE Trans. Instrum. Meas. **54**, 759 (2005).

[12] M. Cetina, A. Grier, J. Campbell, I. Chuang, and V. Vuletić, "Bright source of cold ions for surface-electrode traps", Phys. Rev. A **76**, 041401(R) (2007).

[13] M.N. Gaboriaud and M. Desaintfuscien and F.G. Major, "Absolute measurement of the total number of ions stored in an rf quadrupole trap", Int. J. Mass Spectrom. Ion Phys. **41**, 109 (1981).

[14] H.A. Schuessler and C.H. Holder Jr., "Isotope-selective trapping of rare calcium ions using high-power incoherent light sources for the second step of photo-ionization", J. Appl. Phys. **50**, 5110 (1979).

[15] H. Lehmitz, J. Hatterndorf-Ledwoch, R. Blatt, and H. Harde, "Population trapping in excited yb ions", Phys. Rev. Lett. **62**, 2108 (1989).

[16] A. Bauch, D. Schnier, and C. Tamm, "Collisional population trapping and optical deexcitation of ytterbium ions in a radiofrequency trap", J. Mod. Opt. **39**, 389 (1992).

[17] K. Sugiyama and J. Yoda, "Production of YbH^+ by chemical reaction of Yb^+ in excited states with H_2 gas", Phys. Rev. A **55**, R10 (1997).

[18] P. Zhang and A. Dalgarno and R. Côté, "Scattering of Yb and Yb^+", Phys. Rev. A **80**, 030703(R) (2009).

[19] A.T. Grier and M. Cetina and F. Oručević, V. Vuletić, "Observation of cold collisions between trapped ions and trapped atoms", Phys. Rev. Lett. **102**, 223201 (2009).

[20] H.A. Schuessler and C.H. HolderJr. and C.-S. O, "Orbiting charge-transfer cross sections between He^+ ions and cesium atoms at near-thermal ion-atom energies", Phys. Rev. A **28**, 1817 (1983).

[21] J. Yoda and K. Sugiyama, "Ion coulomb crystals: a tool for studying ion processes", Jpn. J. Appl. Phys. **26**, L1780 (1987).

[22] L.S. Brown and G. Gabrielse, "Physics of a single electron or ion in a penning trap", Rev. Mod. Phys. **58**, 233 (1986).

[23] K. Sugiyama, J. Yoda, and T. Sakurai, "Generation of continuous-wave ultravio-

let light by sum-frequency mixing of diode-laser and argon-ion-laser radiation in β-BaB_2O_4", Opt. Lett. **16**, 449 (1991).

[24] S. Urabe, J. Umezu, and M. Ishizu, Oyo Buturi **54**, 964 (1985) (in Japanese).

[25] K. Sugiyama and J. Yoda, "Optical detection of Yb^+ trapped in an rf trap", Hyperfine Interact. **251**, 74 (1992).

[26] K. Jungmann, J. Hoffnagle, R.G. DeVoe, and R.G. Brewer, "Collective oscillations of stored ions", Phys. Rev. A **36**, 3451 (1987).

[27] W. Yang, K. Gao, X. Zhu, J. Wang, L. Shi, J. Li, and G. Huang, "Study of the correlated motion of ion mixtures in an rf ion trap", Z. Phys. D **27**, 199 (1993).

[28] M. Brieger, H. Büsener, A. Hese, F. v. Moers, and A. Renn, "Enhancement of single frequency SGH in a passive ring resonator", Opt. Commun. **38**, 423 (1981).

[29] B. Beier and D. Woll and M. Scheidt and K. J. Boller and R. Wallenstein, "Second harmonic generation of the output of an AlGaAs diode oscillator amplifier system in critically phase matched LiB_3O_5 and β-BaB_2O_4", Appl. Phys. Lett. **71**, 315 (1997).

[30] J. D. Bhawalkar and Y. Mao and H. Po and A. K. Goyal and P. Gvrilovic and Y. Conturie and S. Singh, "High-power 390-nm laser source based on efficient frequency doubling of a tapered diode laser in an external resonant cavity", Opt. Lett. **24**, 823 (1999).

[31] J. D. Bhawalkar and Y. Mao and H. Po and A. K. Goyal and P. Gvrilovic and Y. Conturie and S. Singh, "Efficient frequency doubling of 1-W continuous-wave Ti:sapphire laser with a robust high-finesse external cavity", Appl. Opt. **42**, 1036 (2003).

[32] M. H. Dunn and A. I. Ferguson, "Coma compensation in off-axis laser resonators", Opt. Commun. **20**, 214 (1977).

[33] K. Kato, "Second-harmonic generation to 2048 Å in β-BaB_2O_4", IEEE J. Quant. Electron. **62**, 1013 (1987).

[34] D. Eimerl, L. Davis, and S. Velsko, "Optical, mechanical, and thermal properties of barium borate", J. Appl. Phys. **QE-22**, 1968 (1986).

[35] S. K. Filatov and N. V. Nikolaeva and R. S. Bubnova and I. G. Polyakova, "Thermal expansion of β-BaB_2O_4 and BaB_4O_7 borates", Glass Phys. Chem. **32**, 471 (2006).

[36] H. Kumagai, "Fine frequency tuning in sum-frequency generation of continuous-wave single-frequency coherent light at 252 nm with dual-wavelength enhancement", Opt. Lett. **32**, 62 (2007).

[37] T. W. Hänsch and B. Couillaud, "Laser frequency stabilization by polarization spectroscopy of a reflecting reference cavity", Opt. Commun. **35**, 441 (1980).

[38] G. D. Boyd and D. A. Kleinman, "Parametric interaction of focused gaussian light beams", J. Appl. Phys. **39**, 3597 (1968).

[39] I. Shoji, H. Nakamura, K. Ohdaira, T. Kondo, and R. Ito, "Absolute measurement of second-order nonlinear-optical coefficients of β-BaB_2O_4 for visible to ultraviolet second-harmonic wavelengths", J. Opt. Soc. Am. B **16**, 620 (1999).

[40] K. R. Parameswaran and J. R. Kurz and R. V. Roussev and M. M. Fejer, "Absolute measurement of second-order nonlinear-optical coefficients of β-BaB_2O_4 for visible to ultraviolet second-harmonic wavelengths", Opt. Lett. **27**, 43 (2002).

[41] K. Komori, Y. Takasu, M. Kumakura, Y. Takahashi, and T. Yabuzaki, "Injection-locking of blue laser diodes and its application to the laser cooling of neutral ytterbium atoms", Jpn. J. Appl. Phys. **42**, 5059 (2003).

[42] T. Kohno, M. Yasuda, H. Inaba, and F.-L. Hong, "Optical frequency stability measurement of an external cavity blue diode laser with an optical frequency comb", Jpn. J. Appl. Phys. **47**, 8856 (2008).

[43] D. Das, S. Barthwal, A. Banerjee, and V. Natarajan, "Absolute frequency measurements in Yb with 0.08 ppb uncertainty: Isotope shifts and hyperfine structure in the 399−nm $^1S_0 \rightarrow {}^1P_1$ line", Phys. Rev. A **72**, 032506 (2005).

[44] T. Kohno, M. Yasuda, K. Hosaka, H. Inaba, Y. Nakajima, and F.-L. Hong, "One-dimensional optical lattice clock with a fermionic ^{171}Yb isotope", Appl. Phys. Express **2**, 072501 (2009).

[45] R.E. March and J.F.J. Todd, *Quadrupole Ion Trap Mass Spectroscopy, second edition* (Willey Interscience, 2005).

[46] U. Griesmann and M.A. Baig and S. Ahmad and W.G. Kaenders and B. Esser and J. Hormes, "Photoionization cross sections of doubly excited resonances in ytterbium", J. Phys. B **25**, 1393 (1992).

[47] W. Demtröder, *Laser Spectroscopy* (Springer, 2002).

[48] H. Park, D. Kwon, and Y. Rhee, "Real-time monitoring of Yb vapor density using an extended cavity violet diode laser", Spec. Act. A **60**, 3305 (2004).

[49] C.B. Alock and V.P. Itkin and M.K. Horrigan, "Vapour pressure equations for the metallic elements: 298-2500k", Can. Metall. Q. **23**, 309 (1984).

[50] N.F. Ramsey, *Molecular Beams* (Oxford University Press, 1990).

[51] C.B. Xu and X.Y. Xu and W. Huang and M. Xue and D.Y. Chen, "Rydberg and autoionizing states of neutral ytterbium", J. Phys. B **27**, 3905 (1994).

[52] S.L. Chin and P. Lambropoulos, *Multiphoton Ionization of Atoms* (Academic Press, 1984).

[53] C.J. Dai and S. Zhang and X.W. Shu and D.W. Fang and J. Li, "Pulsed electric-field ionization of stark states of neutral ytterbium", J. Quant. Spectrosc. Radiat. Transfer. **53**, 179 (1995).

[54] F.G. Major and H.G. Dehmelt, "Exchange-collision technique for the rf spectroscopy of stored ions", Phys. Rev. **170**, 91 (1968).

[55] Y. Moriwaki and T. Shimizu, "Effect of a heavy collision partner on ion loss from a radio frequency trap", Jpn. J. Appl. Phys. **344**, 37 (1998).

[56] E.H. Kennard, *Kinetic Theory of Gases* (McGraw-Hill, New York, 1938).

[57] T. Freegarde and J. Coutts, "General analysis of type I second-harmonic generation with elliptical Gaussian beams", J. Opt. Soc. Am. B **14**, 2010 (1997).

Appendix A Characteristics of BBO Crystal

The BBO crystal is usually used in the Type-I phase matching in order to conduct second-harmonic generation, because of a higher efficiency than the Type-II. The phase matching is achieved by rotating the crystal, i.e., angle phase matching. The Type-I phase matching angle $\theta_{\rm m}$ for a negative uniaxial crystal like BBO, derived from the phase matching condition $n_{\rm e}^{2\omega}(\theta_{\rm m})=n_{\rm o}^{\omega}$, is given by

$$\sin^2\theta_{\rm m} = \frac{(n_{\rm o}^{\omega})^{-2} - (n_{\rm o}^{2\omega})^{-2}}{(n_{\rm e}^{2\omega})^{-2} - (n_{\rm o}^{2\omega})^{-2}}\,, \tag{A-1}$$

where $n_{\rm o}$, $n_{\rm e}(\theta)$, $n_{\rm e}$ are refractive indices of the ordinary wave, of the extraordinary wave on the angle θ between the propagation direction and the crystal optic axis, and of the extraordinary wave on $\theta = 90$ degree, respectively, and the superscripts ω and 2ω indicate that the refractive indices are at the fundamental and at the second harmonics, respectively. The walk-off angle ρ is given by [57],

$$\tan\rho = \frac{1-(n_{\rm o}^{2\omega}/n_{\rm e}^{2\omega})^2}{\cot\theta + (n_{\rm o}^{2\omega}/n_{\rm e}^{2\omega})^2\tan\theta}, \tag{A-2}$$

The refractive indices $n_{\rm o}$ and $n_{\rm e}$ of BBO crystal are calculated from the following Sellmeier's equations [33]:

$$\begin{aligned} n_{\rm o} &= \left(2.7359 + \frac{0.01878}{(\lambda/\mu{\rm m})^2 - 0.01822} - 0.01354\,(\lambda/\mu{\rm m})^2\right)^{1/2} \\ n_{\rm e} &= \left(2.3753 + \frac{0.01224}{(\lambda/\mu{\rm m})^2 - 0.01667} - 0.01516\,(\lambda/\mu{\rm m})^2\right)^{1/2} \end{aligned} \tag{A-3}$$

In the SHG at 798 nm, $n_{\rm o}^{\omega}$, $n_{\rm o}^{2\omega}$ and $n_{\rm e}^{2\omega}$ are 1.66, 1.69 and 1.57, respectively. Then, we obtain $\theta_{\rm m} = 29.3^\circ$ and $\rho = 68\,{\rm mrad}\,(= 3.9^\circ)$ from Eqs. (A-1) and (A-2), respectively.

Appendix B Clausius-Clapeyron Equation

The vapor pressure P is empirically estimated as a function of the temperature T by using the Clausius-Clapeyron equation [49]:

$$\log_{10}(P/\mathrm{Pa}) = 5.006 + A + \frac{B}{T/\mathrm{K}} + C \cdot \log_{10}(T/\mathrm{K}), \tag{B-1}$$

where A, B, and C are constants of which values depend on the material. In the case of metallic Yb for the temperature range from 298 K to 2500 K, the values of A, B and C are 9.111, -8111 and -1.0849, respectively.

Acknowledgments

The author appreciates Professor Kitano, Department of Electronic Science and Engineering, Kyoto University, for welcoming me hospitably, continuously guiding me, and giving an opportunity to write the thesis.

The author is deeply grateful to one of my thesis committee members, Professor Kawakami, Department of Electronic Science and Engineering, Kyoto University, for the advice, suggestions, and introducing me to complete the work.

The author is deeply grateful to one of my thesis committee members, Associate Professor Sakai, Department of Electronic Science and Engineering, Kyoto University, for the advice, suggestions, and encouraging me continuously in my work.

The author wishes to thank Professor Yoshiro Takahashi, Department of Physics, Kyoto University, for many helpful advices and evaluation of my work. His helpful questions enable me to consider my work from different perspective.

The author wishes to express my sincere gratitude to my director, Associate Professor Kazuhiko Sugiyama, Department of Electronic Science and Engineering, Kyoto University, for his patience, technical advice and continuously guide of me. The author never forget his efforts and enthusiasm for studying. This makes a tremendous affection for my life.

The author would like to thank Professor Kawakami and Nichia Corporation for providing the ultraviolet laser diode.

The author would like to express my gratitude to Assistant Professor Toshihiro Nakanishi, Department of Electronic Science and Engineering, Kyoto University, for welcoming me hospitably and encouraging me continuously.

The author would like to acknowledge all the members of Kitano Laboratory for supporting me. Without their help, advice, and constant encouragement, this work has

not been completed. In particular, the author would like to express his gratitude to Mr. Hirokazu Kobayashi, Mr. Tomoyuki Uehara, Mr. Yasuhiro Tamayama, Mr. Shuhei Tamate, Mr. Yasutaka Imai, and Mr. Masatoshi Mitaki for their encouragement and useful advice.

The author would like to thank Ms. Keiko Yamada and Ms. Hisako Sekiguchi for the assistance with office processing.

This material is partly supported by the Grant-in-Aid for Scientific Research (No. $20 \cdot 6222$) and by the Global Center of Excellence program, "Photonics and Electronics Science and Engineering" at Kyoto University, from the Japan Society for the Promotion of Science (JSPS).

The author would like to thank my friends, Mr. Toshiyuki Kawaharamura, Mr. Kazunobu Kojima, Mr. Yudai Kamada, Mr. Kazunori Ichikawa, for caring about my work and encouraging me.

My father, grand mother, and late grand father give me a financial support and encourage me continuously. That enables to the author concentrate in my academic work. My brother, and my sister-in-law understand my academic career and their daughter give me the best smile.

List of the author's work

Scientific paper

(1) Y. Onoda, M. Ikeda, K. Sugiyama, H. Yokoyama, and M. Kitano. "Maximization of second-harmonic power using normal-cut nonlinear crystals in a high-enhancement external cavity," Appl. Opt. **48,** 1366 (2009).

(2) Y. Onoda, K. Sugiyama, M. Ikeda, and M. Kitano. "Loading rate of Yb^+ loaded through photoionization in radiofrequency ion trap," Appl. Phys. B, (accepted, 2011).

(3) Y. Onoda, K. Sugiyama, and M. Kitano. "Selective detection of minor isotope lines in saturated absorption spectroscopy by using absorption filtering of major isotope," Opt. Rev. **18,** no. 4, 365 (2011).

Other scientific paper

(1) Y. Onoda, M. Kimura, "Apparent Isotope Shifts Observed by Two-Step Optogalvanic Spectroscopy," J. Phys. Soc. J. **75,** 115002 (2006) Nov.

International conference talk

(1) Y. Onoda, Y. Muroki, M. Nishizaki, S. Kawajiri, Y. Imai, K. Sugiyama, and M. Kitano, "Trapping of Yb^+ ions produced by photoionization and detection by electric resonance method," 1st Young Researchers International Symposium, Kyoto, Japan, October 31 (2008), oral.

(2) Y. Onoda, K. Sugiyama, and M. Kitano, "Loading Rate of Photoionized Yb^+ Measured with Electric Resonance Method," AP-RASC'10, Toyama, Japan, A3a-2,

September 24 (2010), oral.

List of domestic conference talks

(1) 小野田有吾, 池田充彦, 杉山和彦, 北野正雄, "光イオン化法で生成した Yb^+ のイオントラップ" (26aQD-9), 第 63 回日本物理学会, 近畿大学 (2008 年 3 月 22 日–3 月 26 日)

(2) 小野田有吾, 杉山和彦, 池田充彦, 北野正雄, "光イオン化法で生成した Yb^+ の RF イオントラップへの導入速度", 第 65 回日本物理学会, 岡山大学 (2010 年 3 月 20 日–3 月 30 日).